Evaluation of the integration of the Wind-Induced Flutter Energy Harvester (WIFEH) into the built environment: Experimental and numerical analysis ☆

Angelo I. Aquino *, John Kaiser Calautit, Ben Richard Hughes

Department of Mechanical Engineering, University of Sheffield, Sheffield S10 2TN, UK

HIGHLIGHTS

- Investigation of WIFEH in wind tunnel and CFD of harvester-building were presented.
- Prototype was built and operation in various wind speeds was tested in wind tunnel.
- Impact of WIFEH locations and wind direction on speed at device were investigated.
- The roof apex showed the highest potential for power generation based on results.
- RMS and peak voltages and SC-current values were obtained for various wind speeds.

GRAPHICAL ABSTRACT
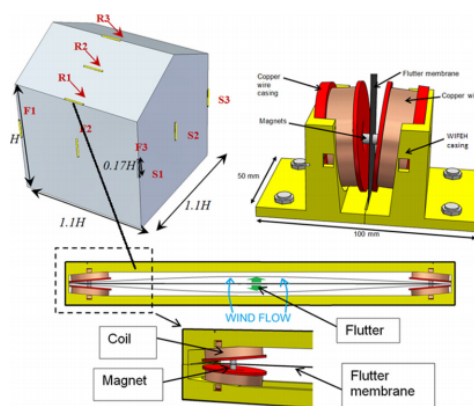
Abstract

With the ubiquity of low-powered technologies and devices in the urban environment operating in every area of human activity, the development and integration of a low-energy harvester suitable for smart cities applications is indispensable. The multitude of low-energy applications extend from wireless sensors, data loggers, transmitters and other small-scale electronics. These devices function in the microWatt-milliWatt power range and will play a significant role in the future of smart cities providing power for extended operation with little or no battery dependence. This study thus aims to investigate the potential built environment integration and energy harvesting capabilities of the Wind-Induced Flutter Energy Harvester (WIFEH) – a microgenerator aimed to provide energy for low-powered applications. Low-energy harvesters such as the WIFEH are suitable for integration with wireless sensors and other small-scale electronic devices; however, there is a lack in study on this type of technology's building integration capabilities. Hence, there is a need for investigating its potential and optimal installation conditions.

This work presents the experimental investigation of the WIFEH inside a wind tunnel and a case study using Computational Fluid Dynamics (CFD) modelling of a building integrated with a WIFEH system. The experiments tested the WIFEH under various wind tunnel airflow speeds ranging from 2.3 to 10 m/s to evaluate the induced electromotive force generation capability of the device. The simulation used a gable-roof type building model with a 27° pitch obtained from the literature. The atmospheric boundary layer (ABL) flow was used for the simulation of the approach wind. The work

investigates the effect of various wind speeds and WIFEH locations on the performance of the device giving insight on the potential for integration of the harvester into the built environment. The WIFEH was able to generate an RMS voltage of 3 V, peak-to-peak voltage of 8.72 V and short-circuit current of 1 mA when subjected to airflow of 2.3 m/s. With an increase of wind velocity to 5 m/s and subsequent membrane retensioning, the RMS and peak-to-peak voltages and short-circuit current also increase to 4.88 V, 18.2 V, and 3.75 mA, respectively. For the CFD modelling integrating the WIFEH into a building, the apex of the roof of the building yielded the highest power output for the device due to flow speed-up maximisation in this region. This location produced the largest power output under the 45° angle of approach, generating an estimated 62.4 mW of power under accelerated wind in device position of up to 6.2 m/s. For wind velocity (UH) of 10 m/s, wind in this position accelerated up to approximately 14.4 m/s which is a 37.5% speed-up at the particular height. This occurred for an oncoming wind 30° relative to the building facade. For UH equal to 4.7 m/s under 0° wind direction, airflows in facade edges were the fastest at 5.4 m/s indicating a 15% speed-up along the edges of the building.

Keywords

Aero-elastic flutter; Buildings; Computational Fluid Dynamics (CFD); energy harvesting; wind tunnel

1. Introduction

In this day and age, buildings are attributed for 20-40% of total world power consumption. This is a figure greater than the consumptions of industry and transport sectors [1]. Thus, new technologies that can mitigate the building sector power demand are increasingly being advanced; one significant advancement being wind energy technology. An important value of building-integrated wind energy harvesting is bringing the power plant closer to the power consumers. With the public having better power generation capabilities, people can also expect better energy efficiency and reduced dependence to power companies, lower carbon footprint and general stimulation of the economy. Moreover, this shift will decrease the load of the grid, dependence on diesel generators in events of power outage and lower transmission costs.

However, urban and suburban locations present problems for conventional building-mounted turbines. There is the issue of significant turbulence in these areas, impeding the turbines from harnessing laminar wind flow. In these conditions wind turbine installers face insufficiency in analysing the more complex wind conditions. This leads to problems of unfavourable turbine site selection leading to deficient power production. Another issue that conventional rotational turbines face is the hazard of having blades flying loose. These aspects add to the anxiety of turbine installation among building owners, residents and stakeholders. However, perhaps the biggest issue to building-integrated wind turbines (BIWT) is their cost-effectiveness. Smaller wind turbines suitable for urban installations when installed onto buildings allow for a higher cost-to-energy-production ratio.

A novel and emerging alternative to the conventional turbines are wind-induced flutter energy harvesters. In this day and age, low-energy power generation devices have been gathering increased attention because of their potential integration with self-

2

powered micro-devices and wireless sensor networks especially in the urban setting. This is a primary motivation for this study. The power produced by these microgenerators is sufficient to run light-emitting diodes, stand-alone wireless sensor nodes and small liquid crystal displays [2]–[4]. Such devices like the Wind-Induced Flutter Energy Harvester (WIFEH) as shown in Figure 1 can be in a form of a small-scale wind generator that takes advantage of the flutter effect. Unlike turbine-based generators, the WIFEH is a small-scale, light and inexpensive direct-conversion energy harvester which does not use any gears, rotors or bearings. Wind flowing into and around a tensioned membrane or belt causes it to flutter causing connected permanent magnets to vibrate relative to a set of coils. This motion induces a current flowing in the coil, thereby generating electric power.

Fig 1. Schematic diagram of a quad (4-coil arrangement) Wind-Induced Flutter Energy Harvester (WIFEH)

The phenomenon of aero-elastic flutter describes self-feeding oscillations in which the aerodynamic forces on a structure couple with its natural mode of oscillation thereby producing rapid periodic movements. Flutter can occur to any structure exposed to strong fluid flow, under the condition that a positive feedback response results between the structure's natural vibration and the acting aerodynamic forces [8].

Flutter on itself can be severely disastrous. Historic examples of flutter are the collapse of Tacoma Narrows Bridge and that of Brighton Chain Pier. The structures failed due to span failure caused by aero-elastic flutter [5]. However, this seemingly violent nature of flutter can also be the foundation of its power when its potential for energy harnessing is investigated. Flutter is classified under flow-induced vibrations, which is an umbrella category that includes flutter-induced vibrations (FIV) [6]–[8] and vortex-induced vibrations (VIV) [9]–[11].

Regular wind turbines generally don't scale down well into smaller scales. Nevertheless, flutter-based generators like the WIFEH can be designed to be suitable for lighter applications. Low-energy flutter-based generators can operate in the range of milliWatt to microWatt power generation. Although the power output is low, it has its advantages compared to traditional wind turbines. The WIFEH is small, compact, modular and suitable for turbulent flow, making it appropriate for partnering with wireless sensor technologies – a field which has the greatest application potential for this energy harvester [12]. Flutter energy harvesting is also not limited to electromagnetic transduction, but can also be taken advantage of through the use flexible piezoelectric membranes as demonstrated with an inverted flag harnessing ambient wind to power a temperature sensor [13].

Recent world demand for wireless sensors is growing particularly in applications of equipment supervision and monitoring focused on energy expenditure, usage, storage and remote manipulation. The principal difficulties to what we call the "deploy-and-forget" nature of wireless sensor networks (WSNs) are their restricted power capacity and their batteries' unreliable lifetimes. To surmount these problems, the area of energy harvesting of ambient energy resources like air flow, water flow, vibrations, and even radio waves has developed to be an encouraging new field. These and several

3

120 other types of ambient energy sources have been harnessed through various
121 technologies like thermomechanical, thermoelectric, photovoltaic and wind harvesting
122 technology [14]. There are even initiatives to develop micro-energy harvesters that can
123 harness both physical and chemical energies of the human body to power implanted
124 biomedical devices [15]. Along with developments in microelectronics, power
125 requirements for wireless sensor nodes keep on falling, varying presently from
126 microWatts to a few milliWatts [12].

128 In the year 2011, more than 1 million units of harvester modules were bought around
129 the world for building applications alone. This was mainly attributed to the expansive
130 network of wireless switches dedicated for lighting, air conditioning and sensors
131 detecting resident presence and determining ambient room conditions such as
132 humidity and temperature, mostly realised in commercial buildings. Running the
133 market growth of energy harvesters are the significant savings in installation costs and
134 maintenance-free operability due to little or no wire installation requirement [16].
135 Hence, novel methods should be established to further assess and optimise energy
136 harvester integration into the built environment. It has been shown that simple
137 configuration, low production cost and fast prototyping coupled with 3D-printing
138 technology all contribute to demonstrate practical applications of mini airflow-driven
139 energy harvesters in the urban setting [17].

141 In this paper, the evaluation of the energy harnessing potential of the WIFEH is
142 discussed. The evaluation is done two-fold: (i) through experimental investigation of
143 the harvester prototype conducted inside a wind tunnel; and (ii) through CFD analysis
144 relating external conditions and harvester location to harvester power generation
145 capabilities. The experimental analysis will assess a constructed WIFEH prototype's
146 performance when subjected to different wind tunnel airflow velocities. The prototype
147 will be centrally mounted with the membrane allowed to flutter in the wind thereby
148 inducing relative motion between fastened permanent magnets and a fixed conducting
149 coil. This motion in turn induces an electromotive force (voltage) in the conducting coil.
150 The (root-mean-square) RMS and peak-to-peak voltages and current readings will be
151 recorded through a memory-enabled digital oscilloscope and afterwards analysed and
152 discussed.

154 Brief review of previous works on the WIFEH exposed that several authors have
155 assessed the performance of the device in uniform flows in the laboratory or wind
156 tunnel but did not investigate the effect of buildings on its performance. Therefore it is
157 evident that there exists the necessity of investigating the integration of the WIFEH into
158 buildings using CFD analysis.

160 The CFD analysis will investigate the effect of various external conditions and device
161 locations on the performance of the WIFEH. The simulation will use a gable-roof type
162 building model with a 27˚ pitch. The atmospheric boundary layer (ABL) flow will be
163 used for the simulation of the approach wind. The three-dimensional Reynolds-
164 averaged Navier-Stokes (RANS) equations along with the momentum and continuity
165 equations will be solved using ANSYS FLUENT 16 for obtaining the velocity and
166 pressure field. Sensitivity analyses for the grid resolutions of the CFD simulations will
167 be performed for verification of modelling. In addition, the results of the flow around the

168 buildings and surface pressure coefficients will be validated with previous experimental
169 work. Figure 2 shows the overview of how this study is organised.
170
171   Fig. 2. General organisation of the study

172 Section 1 introduces the overview of the project, the motivation, challenges, a brief
173 background of the technology and the direction of the research. Section 2 presents the
174 review of related literature. Section 3 discusses the experimental aspect of the study
175 evaluating the technology prototype inside a wind tunnel, while Section 4 presents the
176 results of CFD analysis of the device integration into buildings. Section 5 highlights the
177 key findings.

178 **2. Literature Review**

179 In this section, various relevant energy harvester technologies for flow-induced flutter
180 focusing on the electromagnetic generation principle are reviewed.
181
182 Pimentel et al. [18] investigated the operation of a wind flutter harvester via
183 experimental testing. The evaluated device was 50-cm long and supported by a
184 Plexiglass frame, with a tensioned Mylar membrane installed with bolts on its ends.
185 This membrane had one side that is smooth while the other side was rough. This is
186 analogous to a simple aerofoil. The generator had an electromagnetic transducer
187 integrated in one end of the membrane. This transducer utilised two small neodymium
188 (NdFeB) magnets and a static coil situated adjacent to the magnets. Based on the
189 investigators' experimental results the minimum power output was 5 mW at wind speed
190 of 3.6 m/s and load resistance of 10 Ω; the maximum power output was 171 mW under
191 airflow of 20 m/s, 110 Ω resistance and 38.1 N membrane tension.
192
193 Several parameters that affect the wind flutter harvester performance like membrane
194 tension, membrane length, magnet position and number of magnets were investigated
195 by Arroyo et al. [19] using experimental methods. The study highlighted the optimal
196 values for the key parameters, focusing on low wind speeds ranging from 1 to 10 m/s
197 but with powerful vibration acceleration. Dinh Quy et al. [20] studied a wind flutter
198 harvester with the magnet positioned centrally along the flexible membrane made of a
199 type of kite fabric called ripstop nylon fabric. The single unit micro generator was able
200 to produce power in the range of 3 - 5 mW. Five larger versions of these
201 microgenerators were combined to produce a "windpanel", which altogether were able
202 to deliver 30 to 100 mW of power at wind speeds less than 8 m/s. At low wind speeds
203 between 3 to 6 m/s, the output current is approximately 0.2 to 0.5 mA, the generated
204 voltage is between 2 to 2.5 V, and the generated power is about 2 to 3 mW, under
205 membrane oscillation frequency of approximately 5 Hz.
206
207 The earlier generations of flutter generators encountered practical problems as
208 identified by Fei et al. [21]. One example was the physical contact of the vibrating
209 membrane with the coils when its vibration amplitude is at an extreme high during
210 powerful winds. The placing of the magnets on the membrane should be thoroughly

tested to guarantee optimised magnetic flux undergone by the coils, which was also addressed by Dinh Quy et al. [20].

To deal with these challenges and at the same time increase the efficiency of energy harvesting by a fluttering belt, a novel variety of flutter-based resonant system was proposed in [21] which involves of a shaft that acts as a support, an electromagnetic resonator, a power management circuit, a super-capacitor for storage of charge and a spring. A belt with dimensions 1 m long, 25 mm wide and 0.2 mm thick polymer was used as the oscillating membrane. The electromagnetic resonator was positioned close to the end of the membrane. This was the selected placement because of a higher bending stiffness of the membrane close to the secured ends. This configuration permitted a heavier magnet to be supported by the vibrating membrane [21]. The super-capacitor is simply replaceable.

Dibin Zhu et al. [22] studied a device with an aerofoil linked to a beam which was located next to a bluff body. This energy harvester worked under relatively low airflow speed of 2.5 m/s and produced power of 470 µW. The investigators found that a drawback of this system was the factor that an initial displacement of the aerofoil was required in order to be activated. Wang et al. [23] demonstrated a type of EMG-resonant-cavity wind energy harvester integrated with dual-branch reed and tuning fork vibrator. Their study emphasised the harvester's magnetic circuit being able to increase the rate of change of magnetic flux. The tuning-fork mechanism of the harvester was able to reduce system losses. Apex power output was measured to be 56 mW corresponding to a wind speed of 20.3 m/s with efficiency of energy conversion of 2.3% at wind speed of 4 m/s. The experimental tests verified that the harvester can operate in a wide range of wind speeds.

Two types of electromagnetic energy harvesters were investigated by Kim et al. [24] which utilise direct airflow energy conversion to mechanical vibration - (i) a wind-belt-like oscillatory linear energy collector specially for powerful air streams and (ii) a harvester involving a *Helmholtz resonator* concentrated on harvesting energy from weaker airflow like those found in environmental air streams. The moving part of the harvester was made up of an oscillating membrane with secured permanent magnets, positioned in the centre of the airflow. The second energy collector utilised a Helmholtz resonator as an apparatus for concentrating oncoming wind flow. The wind-belt-like oscillatory energy collector offered a peak-to-peak amplitude AC voltage of 81 mV at frequency of 530 Hz, generating this from an input of 50 kPa of pressure. The Helmholtz-resonator-centred harvester provided a peak-to-peak amplitude AC voltage of 4 mV at frequency of 1400 Hz, from 0.2 kPa pressure input, which corresponded to 5 m/s or 10 mph airflow speed.

253 It was demonstrated by Munaz et al. [25] that the energy generation of electromagnetic
254 energy harvester can be amplified by several factors through the introduction of
255 numerous magnets as the moving mass despite the fact that all other experimental
256 parameters were fixed. The harvester generated power of 224.72 µW in rectified DC
257 already, while having a load resistance of 200 Ω for a five-magnet setup. This
258 electromagnetic energy harvester operated at a low resonance frequency of 6 Hz,
259 which was envisioned by the investigators to be suitable for handheld devices and
260 remote sensing applications.
261
262 Energy harvesting through vibrations caused by the Karman vortex street through an
263 electromagnetic harvester was investigated by Wang et al. [6], with a device able to
264 produce instantaneous power of 1.77 µW when exposed to the vortex street. The open
265 circuit peak-to-peak voltage induced in the coil was measured to be approximately 20
266 mV. In the same investigation the researchers acknowledged that the vibrations from
267 other fluid flow can also be harnessed such as river currents, air flow from tire or fluids
268 inside machinery.
269
270 Kwon et al. performed an investigation for energy harvesting devices that use
271 T-shaped cantilever intended to accelerate the occurrence of aero-elastic flutter for low
272 wind speeds. The investigators studied two device types – one working through
273 piezoelectric effect while the other operates under electromagnetic induction principle.
274 For the electromagnetic energy converter the cantilever is permitted to undergo flutter
275 thereby causing the motion of magnets with respect to coils, producing electricity in the
276 conducting coils. The devices were tested inside a wind tunnel and it was observed
277 that the electromagnetic converter was able to generate a maximum of 1.2 mW of
278 power under 10 m/s wind speed, while the piezoelectric device provided 1.5 mW
279 maximum power [26].
280
281 Park et al. investigated a technology with a funnel that was intended to contract wind
282 flowing towards the energy harvester. The study noted that aero-elastic flutter
283 phenomenon only starts when airflow speed reaches a specific flutter onset speed and
284 when airflow is nearly perpendicular to the harvester. The investigators' solution was
285 to introduce a wind-flow-contracting funnel conceived to channel airflow to the flutter
286 energy converter and accelerate the airflow. The authors compared the device
287 performance under varying incident angles of wind and its effect on the voltage
288 generation for the device versions with funnel and without funnel. With the funnel, the
289 harvester produced almost a constant voltage even when the incident wind flow angle
290 varied. The initial CFD and wind tunnel results also exhibited that the funnel can
291 accelerate airflow speed by an estimated 20% within an incident angle of 30⁰ [27].
292
293 In another study by Arroyo et al. two significant parameters namely the critical flutter
294 frequency and the critical wind speed as functions of the ribbon dimensions and
295 material properties were focused on through utilising both theoretical modelling and

experiments. The important finding was that from both simulation and experiments, the critical speed increased when the dimensions were reduced. Therefore a device designed for low-speed airflow has to take into account this increase through marginally decreasing the ribbon tension since the higher the ribbon tension is, the greater the airflow speed required to start fluttering [28].

No previous work reviewed the integration of low-energy flutter-induced harvesting devices in buildings or structures. Most studies for these energy harvesters were carried out in laboratory environments. There is also a lack in numerical investigations about these energy harvesting technologies. There is a deficiency in research about the applications of these harvesters in the urban environment. Most theoretical studies employ unrealistic boundary conditions like the use of uniform flows. This study will address this by conducting an urban flow simulation of a small building integrated with low-energy wind-induced flutter energy harvester devices and evaluate the impact of varying outdoor wind conditions.

Prior investigations about the building environment's potential for wind energy harvesting underlined the necessity for detailed and precise analysis of wind flow around buildings. To exploit the effect of wind acceleration above or around buildings and to be able to determine the applicable type of wind energy technology to be installed, appropriate integration analysis has to be conducted. In addition, there exists the challenge of analysing the optimum placement of the wind energy harvesters. Thorough simulations will lead to more data that can result to better installation decisions [29].

3. Performance evaluation of WIFEH prototype using wind tunnel testing

To characterise the effect of various wind speeds to the harvester's performance, a prototype was constructed and tested inside the wind tunnel. The prototype was tested under varying wind tunnel airflow speeds to enable the measurement of RMS voltage, peak-to-peak voltage and short-circuit current generated by the harvester in response to the different wind velocities.

A full scale model of the WIFEH prototype was used in the experimental study. The investigation was conducted in a low-speed closed-loop wind tunnel detailed in [30]. The wind tunnel had a test section with the dimensions of 0.5, 0.5, and 1 m (see Figure 3). The variable intensity axial fan is capable of supplying wind speeds between 2.3 to 12 m/s. The flow in the wind tunnel was characterised prior to experimental testing to indicate the non-uniformity and turbulence intensity in the test-section which was 0.6% and 0.49% and according to the recommended guidelines [30].

Fig. 3. (a) Side view of the closed-loop wind tunnel (b) WIFEH prototype with one coil configuration showing flutter motion at 2.3 m/s

The WIFEH system with one coil and eight stacked 1.5 mm-thick 10 mm-diameter magnets was tested for preliminary experimental results inside the wind tunnel. The prototype was positioned in a vertical orientation with terminals, as shown in Figure 4.

341 For data gathering, the system was connected to the digital oscilloscope positioned
342 outside the wind tunnel. It was ensured that the wind tunnel did not contain anything
343 except the WIFEH. The wind speed inside the tunnel was varied from the wind tunnel
344 minimum of 2.3 m/s to maxima of (i) 8 m/s without belt retensioning and (ii) 10 m/s with
345 belt retensioning. It should be noted that without retensioning, the performance of the
346 belt did not improve beyond 8 m/s. Without membrane retension there was observed
347 self-sustained but unstable oscillations leading to irregular voltage signal readings.
348
349   Fig. 4. Schematic of WIFEH prototype in the wind tunnel test section
350
351 The WIFEH was then connected to the Tektronix Oscilloscope to measure, display and
352 record the system's AC (Alternating Current) voltage output. This is depicted in
353 Figure 5. The voltage waveform relevant characteristics such as the maximum value,
354 peak-to-peak voltage, root-mean-square (RMS) voltage and frequency could be
355 observed instantaneously in the 7-inch WVGA TFT colour display monitor. The
356 Tektronix TBS1052B Digital Storage Oscilloscope model is capable of up to 1 GS/s
357 sampling rate, bandwidths of 50 - 200 MHz and has a dual channel frequency counter.
358 The instrument has 3% vertical (voltage) measurement accuracy permitting the user
359 to see all signal details and obtain the stated real-time sampling rate on all channels
360 all the time with at least 10X over sampling; sampling performance is not reduced when
361 changing the horizontal (time) scale. The oscilloscope has two probes that were
362 attached to the two ends of the coils of the energy harvester, with one probe also
363 connected to the ground, to measure the potential difference between two points at
364 each specific time. Measurements were taken uninterruptedly producing a continuous
365 waveform that is displayed in oscilloscope's LCD monitor and were recorded in a
366 storage device connected to the oscilloscope USB port.
367
368   Fig. 5. Schematic of the coil connections to the oscilloscope
369
370 The WIFEH model used for the wind tunnel testing was partially constructed using 3D
371 printing. The schematic diagram of the two-coil prototype system is shown in Figure 6.
372 The copper wire used to make the conducting coil is enamelled copper wire 40 SWG
373 (Standard Wire Gauge) with 0.125 mm diameter. It is packaged as grade 1 enamelled
374 copper wire in a roll of 250 grams and is suitable for coil forming. This copper wire is
375 tested based on the standards of IEC 851/5/4 having a threshold energy transfer rate
376 of 7 kVA (kilovolt-Amperes). The circular casing was 3D-printed using HP Designjet
377 3D Printer. The outer diameter of the casing is 54 mm and the inner diameter (hole
378 diameter) is 12.5 mm, with outer thickness of 20 mm and inner spacing for the coil
379 winding of 12 mm. The two ends of the coil wire were soldered onto insulated jumper
380 lead wires for more convenient connections to the load (LED) for initial testing of
381 generation, circuit board or testing apparatus. Approximately 2500 turns were looped
382 to produce the coil. The internal resistance of the coil is 1150 Ohms.
383
384 The flexible membrane is made of a two layer construction: a weather-resistant outer
385 shell and reinforced fabric backing. It resists moisture, UV rays and extreme
386 temperature. The backing material provides strength due to the tight weave. It adheres
387 to metallic objects well. It is highly suitable to hold the magnets in place, sturdy but light
388 and highly flexible allowing flutter to occur. In the tests it has not let the magnets fall
389 off in any trial done. A 1 cm wide section of the tape material of which 0.5 m in length
390 was exposed to airflow was used for the harvester. These dimensions were observed

to be suitable for the flutter occurrence to be initiated with the given load of the magnets while keeping the use of the tape material economically, thereby reducing its weight.

Neodymium N52 type disk magnets were used to generate the magnetic fields that are going to interact with the conducting coils. The magnets have a diameter of 10 mm and a thickness of 1.5 mm. N52 is the highest grade for magnets that are widely available. In a size for size comparison an N52 grade magnet will have approximately 35% more pull power than the same sized N35 grade magnet. This type of magnet is axially magnetised through the thickness producing one surface as the North pole and the other surface being the south pole. Each unit weighs 0.09 g and has a coating of Ni-Cu-Ni layers (Nickel-Copper-Nickel). The calculated maximum vertical hold of each magnet is 206 g, having a theoretical maximum pull of 1033 g. The maximum operating temperature of this type of magnet is 80°C, beyond which it will start to lose part of its magnetisation. Four units of the 1.5 mm thick magnets were stacked together which are then attached to the adhesive side of the belt. It was estimated that four stacked magnets will possess sufficient magnetic field strength strong enough to generate substantial induction in the coils but at the same time not too heavy to hinder the belt flutter motion. To balance the four magnets on one side, another four were attached on the other side of the membrane with the opposite pole facing the first magnets stack so that the magnetic attraction kept the two magnet groups in place.

Fig. 6. Schematic and dimensions of 3D-printed WIFEH prototype

The AC Voltage waveform produced by the WIFEH system when subjected to a constant airflow of 2.3 m/s is shown in Figure 7, forming a regular pattern of sinusoidal wave. This first trial corresponds to the initial and minimum flow velocity of the wind tunnel. The root-mean-square (RMS) voltage was measured to be 3.00 V. The RMS voltage is the effective value of a varying voltage source such as the WIFEH. The rated output of most power supplies are expressed in RMS AC voltage (e.g. 110 / 230 V wall socket output is RMS value). The maximum voltage reading was 3.84 V while the peak-to-peak voltage was 8.72 V.

Fig. 7. Open-circuit voltage of the Wind-Induced Flutter Energy Harvester (WIFEH) without membrane retensioning under 2.3 m/s flow velocity

Without prior retensioning the membrane, the wind tunnel airflow speed was increased to 5 m/s and the AC voltage signal was again observed and recorded as shown in Figure 8. The waveform is not as regular as for the previous case and we can observe more occurrences of sharper turns with resemblance to sawtooth signals, with decreasing magnitude of the negative peaks of the signal. The recorded RMS for 5 m/s wind speed is 4.16 V with peak-to-peak value 18.4 V and maximum value of 8.8 V.

Fig. 8. Electrical signal open-circuit voltage of the Wind-Induced Flutter Energy harvester (WIFEH) without membrane retensioning under 5m/s flow velocity

The membrane of the WIFEH was then retensioned while maintaining the wind tunnel airflow speed of 5 m/s. The AC Voltage waveform produced by the harvester system when subjected to a constant airflow was again recorded. A regular pattern of sinusoidal wave with minor and major peaks was again observed. Under this wind

440 condition, the microgenerator generated an RMS voltage of 4.88 V with maximum of
441 9.20 V and peak-to-peak value of 18.2 V. This is shown in Figure 9.
442
443   Fig. 9. Electrical signal open-circuit voltage of the Wind-Induced Flutter Energy
444   Harvester (WIFEH) with membrane retensioning under 5 m/s flow velocity
445
446 Incremental increases of 1 m/s airflow speed were also conducted for two cases: (i)
447 without belt retensioning (see Figure 10) and (ii) with belt retensioning (see Figure 11),
448 starting from 2.3 m/s. The open-circuit voltage and short-circuit current were then
449 observed using a digital multimeter after each incremental increase. The digital
450 multimeter used was the Proster VC99. It is an auto-ranging digital multimeter capable
451 of measuring AC/DC voltage and current, resistance, frequency and duty cycle, which
452 provides an LCD display.
453
454 It can be observed that for the case without belt retensioning the maximum open-circuit
455 voltage and short-circuit current both occurred for 6 m/s airflow speed, beyond which
456 there was a significant drop in both variables. This was due to the observation that
457 beyond said airflow speed the belt started to perform less stable oscillations compared
458 to cases of lower wind speeds. This unstable flutter greatly influences the magnets-
459 coil relative dynamic positioning, therefore affecting the induced voltage and current in
460 the conducting coil. Thus the relationship between airflow speed and open-circuit
461 voltage or short-circuit current was not observed to be linear (Figure 9). However, with
462 retensioning of the belt the linear relationship between airflow and voltage / current
463 resumed as can be seen in Figure 10. The trend continued even up to 10 m/s airflow
464 speed.
465
466   Fig. 10. Electrical output performance of the WIFEH without retensioning under
467   various flow velocities: (a) Open-circuit voltage (b) Short-circuit current
468
469
470   Fig. 11. Electrical output performance of the WIFEH with retensioning under various
471   flow velocities: (a) Open-circuit voltage (b) Short-circuit current
472

4. Computational Fluid Dynamics (CFD) analysis of WIFEH integration into buildings

475 The basic assumptions for the numerical simulation include a three-dimensional, fully
476 turbulent, and incompressible flow. The flow was modelled by using the standard
477 k-epsilon turbulence model, which is a well-established method in research on wind
478 flows around buildings [31], [32]. The CFD code was used with the Finite Volume
479 Method (FVM) approach and the Semi-Implicit Method for Pressure-Linked Equations
480 (SIMPLE) velocity-pressure coupling algorithm with the second order upwind
481 discretisation. When the flow is not aligned with respect to the grid, more accurate
482 results are generally obtained by using the second order discretisation, especially
483 when dealing with complex flows. The general governing equations include the
484 continuity, momentum and energy balance for each individual phase. The standard k-
485 e transport model was used to define the turbulence kinetic energy and flow dissipation
486 rate within the model. The governing equations for the mass conservation (eqn. 1),
487 momentum conservation (eqn. 2), energy conservation (eqn. 3), turbulent kinetic
488 energy (TKE) (eqn. 4) and energy dissipation rate (eqn. 5) are summarised below:

11

489

$$\frac{\partial \rho}{\partial t} + \nabla \times (\rho u) = 0 \qquad \text{(eqn.1)}$$

490 where ρ is density, t is time and u is fluid velocity vector.

$$\frac{\partial (\rho u)}{\partial t} + \nabla \times (\rho u u) = -\nabla p + \rho g + \nabla \times (\mu \nabla u) - \nabla \times \tau_t \qquad \text{(eqn.2)}$$

491 where p is the pressure, g is vector of gravitational acceleration, μ is molecular dynamic
492 viscosity and τ_t is the divergence of the turbulence stresses which accounts for
493 auxiliary stresses due to velocity fluctuations.

$$\frac{\partial (\rho e)}{\partial t} + \nabla \times (\rho e u) = \nabla \times \left(k_{eff} \nabla T \right) - \nabla \times \left(\sum_i h_i j_i \right) \qquad \text{(eqn.3)}$$

494 where e is the specific internal energy, k_{eff} is the effective heat conductivity, T is the air
495 temperature, h_i is the specific enthalpy of fluid and j_i is the mass flux.

$$\frac{\partial (\rho k)}{\partial t} + \nabla \times (\rho k u) = \nabla \times \left[\alpha_k \mu_{eff} \nabla k \right] + G_k + G_b - \rho_\varepsilon \qquad \text{(eqn.4)}$$

$$\frac{\partial (\rho \varepsilon)}{\partial t} + \nabla \times (\rho \varepsilon u) = \nabla \times \left[\alpha_\varepsilon \mu_{eff} \nabla \varepsilon \right] + C_{1\varepsilon} \frac{\varepsilon}{k} (G_k + C_{3\varepsilon} G_b) - C_{2\varepsilon} \rho \frac{\varepsilon^2}{k} \qquad \text{(eqn.5)}$$

496 where G_k is the source of TKE due to average velocity gradient, G_b is the source of TKE
497 due to buoyancy force, α_k and α_ε are turbulent Prandtls numbers, $C_{1\varepsilon}$, $C_{2\varepsilon}$ and $C_{3\varepsilon}$ are
498 empirical model constants.

499 The geometry (Figure 12) was created using commercial CAD software and then
500 imported into ANSYS Geometry (pre-processor) to create a computational model. The
501 shape of the building was based on [32], which is a gable roof type building with a roof
502 pitch of 26.6°. The overall dimension of the building was 3.3 m (L) x 3.3 m (W) x 3 m
503 (H). To create a computational domain, the fluid volume was extracted from the solid
504 model as shown in Figure 13. The fluid domain consisted of an inlet on one side of the
505 domain, and an outlet on the opposing boundary wall. The simulations were completed
506 using parallel processing on a workstation with two Intel Xeon 2.1 GHz processors and
507 16 GB fully-buffered DDR2 memory.

508
509   Fig. 12. CAD geometry of building with WIFEH devices

510 The computational domain size and location of model were based on the guideline of
511 COST 732 [33] for environmental wind flow studies. According to the guidelines, for a
512 single building with the height H, the horizontal distance between the sidewalls of the
513 building and side boundaries of the computational domain should be *5H*. Similarly, the
514 vertical distance between the roof and the top of domain should also be *5H*. In the flow
515 direction, the distance between the inlet and the façade of the building should be *5H*
516 while for the leeward side and outlet, it should be *15H* to allow the flow to re-develop
517 behind the wake region, as fully developed flow is normally assumed as the boundary
518 condition in steady RANS calculations [33] .

519
520   Fig. 13. Computational domain of building with WIFEH devices

521

4.1 Mesh design and verification

522 **4.1 Mesh design and verification**
523 Due to the complexity of the model, a non-uniform mesh was applied to volume and
524 surfaces of the computational domain [34], [35]. The generated computational mesh
525 of the building model is shown in Figure 14. The grid was modified and refined
526 according to the critical areas of interests in the simulation such as the WIFEH. The
527 size of the mesh element was extended smoothly to resolve the areas with high
528 gradient mesh and to improve the accuracy of the results. The inflation parameters
529 were set according to the complexity of the geometry face elements, in order to
530 generate a finely resolved mesh normal to the wall and coarse parallel to it [36].
531
532 Fig. 14. (a) Computational grid (b) Sensitivity analysis
533
534 In this study, Grid Convergence Method (GCI) method was used to verify the
535 computational modelling of the building integrated with the WIFEH. The computational
536 grid was based on a sensitivity analysis which was performed by conducting additional
537 simulations with same domain and boundary conditions but with various gird sizes.
538 The process increased the number of elements between 2.44 (coarse), 3.8 million
539 (medium) and 4.90 million (fine). The computational time associated with running the
540 simulations (converged) with coarse, medium and fine mesh were 5 hours, 8 hours
541 and 10 hours, respectively. The grid resolution was determined taking into account an
542 acceptable value for the wall y+. The log-law, which is valid for equilibrium boundary
543 layers and fully developed flows, provides upper and lower limits of the acceptable
544 distance between the near-wall cell centroid and the wall. The distance is usually
545 measured in the dimensionless wall units, y+. The average y+ values over the
546 windward and the leeward roofs were about 70 and 25 for the coarser grid, and about
547 35 and 15 for the finer grid, respectively. The Grid Convergence Method (GCI) method
548 (based on the Richardson extrapolation method) was selected to estimate the
549 uncertainty due to discretisation [37]–[39]. The procedure detailed in [38] was followed
550 and is summarised below:

551 The first step is to define a representative grid size *h*.

$$h = \left[\frac{1}{C} \sum_{i=1}^{C} (\Delta V_i) \right]^{1/3} \qquad \text{(eqn.6)}$$

552 where *C* is the total number of cells used for the 3D computations and ΔV_i is the
553 volume.

554 The next step is to select three significantly different set of grids, *C* and run simulations
555 to determine the values of key variables, $\emptyset$. In this case, the average value of the
556 airflow velocity in the vertical line in the R1 device was selected as the variable. The
557 size of the grids were C1 (5.90 million), C2 (3.50 million) and C3 (2.00 million), giving
558 *r* values of 1.30 and 1.32.

13

559 The next step is to calculate the apparent order, *p* of the method using the next
560 equation. The equation was solved using fixed point iteration, with the initial guess
561 equal to the first term [38].

$$p = \frac{1}{\ln(r_{21})} |ln|\varepsilon_{32}/\varepsilon_{21}| + q(p)| \qquad \text{(eqn.7)}$$

$$q(p) = ln\left(\frac{r_{21}^p - [1 \times sgn(\varepsilon_{32}/\varepsilon_{21})]}{32 - [1 \times sgn(\varepsilon_{32}/\varepsilon_{21})]}\right) \qquad \text{(eqn.8)}$$

562 where $\varepsilon_{32} = \emptyset_3 - \emptyset_2$ and $\varepsilon_{21} = \emptyset_2 - \emptyset_1$.

563 Finally, the approximate relative error e_a^{21}, extrapolated relative error $\emptyset_{ext}^{21}$ and fine-grid
564 convergence index GCI_{fine}^{21} (eqn.10) are calculated.

565 Table 1 shows examples of the calculation procedure for the three selected grids.
566 According to Table 1, the numerical uncertainty in the fine-grid solution for the velocity
567 at 3.012m was 2.68% which corresponded to ± 0.10 m/s.

568   Table 1. Sample calculations of discretisation error using the GCI method

569 Figure 15 (a) shows the vertical velocity profiles (line with 18 equally distributed points)
570 drawn from the R1 device, which was based on the three set grids. In addition, the
571 extrapolated values, $\emptyset_{ext}^{21}$ are also plotted and was calculated using the following
572 equation:

$$\emptyset_{ext}^{21} = \left(r_{21}^p \emptyset_1 - \emptyset_2\right)/\left(r_{21}^p - 1\right) \qquad \text{(eqn.9)}$$

573 The local order of accuracy *p* ranged from 0.95 to 16.1. The average apparent order
574 of accuracy was used to assess the GCI index values in eqn.11, which is plotted in
575 the form of error bars, as shown in Figure 4b. Based on the fine-grid convergence
576 index, the maximum discretisation uncertainty was 5.87%. The discretisation
577 uncertainty value ranged from 0.31% to 6.61%, with a global average of 1.52%.

$$GCI_{fine}^{21} = \frac{1.25 e_a^{21}}{r_{21}^p - 1} \qquad \text{(eqn.10)}$$

578   Fig. 15. Grid verification using the Grid Convergence (GCI) method. (a) plot of the
579   velocity profiles drawn from a line in the R1 device; (b) fine grid solution, with
580   discretisation error bars computed using the GCI index.

4.2 Boundary conditions
582 The boundary conditions were specified according to the AIJ guidelines [40]. The
583 profiles of the airflow velocity *U* and turbulent kinetic energy (TKE) were imposed at
584 the inlet which were based on [32], with the stream-wise velocity of the approaching
585 flow obeying the power law with an exponent of 0.25 which corresponds to a sub-urban
586 terrain (See Figure 16). The values of *ε* for the k-epsilon turbulence model were
587 acquired by assuming local equilibrium of $P_k = \varepsilon$ [32]. The standard wall functions [41]
588 were applied to the wall boundaries except for the ground, which had its wall functions
589 adjusted for roughness [42]. According to [42], this should be specified by an equivalent

14

590 sand-grain roughness height k_s and a roughness constant C_s. The horizontal non
591 homogeneity of the ABL was limited by adapting sand-grain roughness height and
592 roughness constant to the inlet profiles, following the equation of [43] :

593
$$k_s = \frac{9.793 z_0}{C_s} \qquad \text{(eqn.11)}$$

594 where z_0 is the aerodynamic roughness length of the sub-urban terrain. The values
595 selected for sand-grain roughness height and a roughness constant 1.0 mm and 1.0
596 [32]. The sides and the top of the domain were set as symmetry, indicating zero normal
597 velocity and zero gradients for all the variables at the side ant top wall. For the outlet
598 boundary, zero static pressure was used. The boundary conditions for the CFD model
599 are summarised in Table 2.
600
601
602 Fig. 16. (a) Velocity profile (b) TKE profile of approach wind flow [32]
603
604
605 Table 2. Summary of the CFD model boundary conditions
606
607
608 The convergence of the solution and relevant variables were monitored and the
609 solution was completed when there were no changes between iterations. In addition,
610 the property conservation was also checked if achieved. This was carried out by
611 performing a mass flux balance for the converged solution. This option was available
612 in the FLUENT flux report panel which allows computation of mass flow rate for
613 boundary zones. For the current simulation, the mass flow rate balance was below the
614 required value or <1% of smallest flux through domain boundary (inlet and outlet).

615 **4.3 Method verification and validation**
616 Figure 17 shows a comparison of the result of different turbulence model (k-epsilon
617 standard, k-epsilon realizable and k-omega) for the velocity profile drawn from the
618 vertical line in the R1 device. It can be observed that the k-epsilon standard curve lies
619 between the plots of k-epsilon realizable and k-omega, which is especially noticeable
620 between the heights of 3.005 and 3.015 m. It is obvious that there is an occurring
621 speed-up within the interior zone of the WIFEH device regardless of the turbulence
622 model used, as can be observed from Figure 17 (b). Although shifting to the k-omega
623 model could potentially affect the performance results of the WIFEHs located in the
624 leeward side of the building; a higher set of velocity results could be generated leading
625 to greater output for the devices in case of k-omega model.

626 As observed in Figure 17 (a), a very similar trend can be noticed for different turbulence
627 models particularly the k-epsilon standard and realizable with an average error of 3.9%
628 between the points. The average error between k-epsilon standard and k-omega was
629 6.44. From the velocity contours shown in Figure 17 (b) it can be noticed that the
630 k-epsilon standard model also displays mode distinguishable and more evenly
631 distributed velocities at a lower speed at the wake of the flow behind the structure,
632 compared to the k-omega model. The k-epsilon model provides the standard, mostly
633 accepted results and is more suitable when studying free-shear layers and wake zones
634 while the standard k-omega model is more suitable in the near wall boundary regions.
635

Fig. 17. Sensitivity analysis of turbulence model (a) velocity profile in R1 (b) velocity contours

Figure 18 (a) and (b) show a comparison between the experimental PIV results of [32] and the current modelling results of the velocity distribution around the building model. The results of the airflow velocity close to the windward wall seem to be at a lower speed in the model compared to the PIV results, however a similar pattern was observed for most areas particularly close to the roof. Figure 18 (c) and (d) show a comparison between the prediction of the current model and [32] of the pressure coefficient distribution around the building model. It is to be noted that the contour of Figure 18 (a) also apply to that of (b), while that of Figure 18 (c) apply to (d).

Fig. 18. (a) PIV measurements of velocity [32] (b) velocity distribution in the current model (c) pressure coefficient result [32] (d) pressure coefficient distribution in the current model

4.4 CFD results and discussion

The system of the aero-elastic belt energy harvester integrated into a building was modelled using CFD through ANSYS Fluent simulating the airflow pattern, velocity magnitude and distribution around the building and within and surrounding the energy harvester. This was conducted to allow for optimisation of the positioning of the energy harvester throughout the various building sections. This investigation simulated a gentle breeze, which is category 3 in the Beaufort wind force scale.

Figure 19 shows the velocity contours of a side view cross-sectional plane inside the computational domain representing the airflow distribution around the building integrated with WIFEH. The left hand side of the plot shows the scale of airflow velocity in m/s. The contour plot in the fluid domain is colour coded and related to the CFD colour map, ranging from 0 to 5.9 m/s. As observed, the approach wind profile entered from the right side of the domain and the airflow slowed down as it approached the building and lifted up. Separation zones were observed on the lower windward side of the building and also at the leeward side of the building and roof. Zoomed in views of the velocity distribution around the WIFEH devices R1, R2 and R3 are shown on top of the diagram. The results showed that the shape and angle of the roof had a significant impact on the performance of the WIFEH. In the diagram, it is clear that locating the device at the leeward side of the roof will result in little to no energy generation due to the low wind speeds in this area. However, it should be noted that this was not the case for other wind angles, for example when the wind is from the opposite direction. Therefore, location surveying, wind assessment and detailed modelling are very important when installing devices in buildings. At wind velocity (U_H) 4.7 m/s and 0° wind direction, the airflow speed in R1 was the highest at 4.5 m/s while the lowest was observed for the R2 WIFEH located at the centre of the roof.

Fig. 19. Contours of velocity magnitude showing a cross-sectional side view of the building

16

683 Figure 20 displays the velocity contours of a top view cross-sectional plane inside the
684 computational domain representing the airflow distribution around the building
685 integrated with WIFEH. The approach wind profile entered from the right side of the
686 domain and the airflow slowed down as it approached the building and accelerated as
687 it flowed around the corners. Separation zones were observed on the leeward side of
688 the building and also the sides. Zoomed in views of the velocity distribution around the
689 WIFEH devices F1-F3 and S1-S3 are shown on top and right side of the diagram. At
690 wind velocity (U_H) 4.7 m/s and 0° wind direction, the airflow speed in F1 and F3 were
691 the highest at 5.4 m/s while the lowest was observed for the S2 and F2 WIFEH located
692 at the airflow recirculation zones.

693   Fig. 20. Contours of velocity magnitude showing a cross-sectional top view of the
694   building

695 Figure 21 compares the maximum air velocity speed measured at the belt location for
696 roof installations R1, R2 and R3 at various wind directions. These setups behaved in
697 a trend similar to each other, but the notable highest velocities were attained from the
698 R3 or apex installation. These setups had peak velocity values occurring at the region
699 between 30˚ to 60˚ orientation, with the maximum value obtained at 30˚. There was
700 significant speed decrease after 60˚ that could be attributed to the belt frame corners
701 which impeded the wind from flowing through the belt region and therefore would
702 reduce its performance or not allow the belt to flutter

703   Fig. 21. Effect of wind direction on the wind speed at WIFEH located on the roof for
704   various wind angle of approach with outdoor wind U_H = 10 m/s

705
706 Figures 22 and 23 compare the maximum air velocity speed measured at the device
707 location for the windward and side installations, respectively at various wind directions.
708 When comparing the two figures it was observed that the plot of F3 had a similar trend
709 with the S1 device which showed a significant performance drop in terms of velocity
710 between 20-60˚. This was also due to the frame of the WIFEH which impeded the wind
711 from flowing through the belt region and therefore would reduce its performance or not
712 allow the belt to flutter.

713
714 While the plot of F1 was a mirrored of S3, and F2 was mirrored S2. There is some
715 symmetry that can be expected as observing the locations in Figure 12. It is not a
716 perfect symmetry due to the roof shape having some effect on airflow. Looking at the
717 location with highest velocity values for the front side of the building, there was a
718 significant decrease in velocity from 10˚ to 40˚, accounting for approximately 83%
719 speed reduction, and same increase in speed was observed from 40˚ to 70˚. For the
720 side installation S1 the tipping point was at 50˚ where the change in angle exposure
721 past this point marked significant increase in velocity. From the results it was clear that
722 both the location of the device and wind direction had a significant effect on the air
723 speed achieved at the device location. Therefore a complete detailed analysis of these
724 factors should be carried out when integrating WIFEHs to buildings to ensure that the
725 performance is optimised.

17

726 Fig. 22. Effect of wind direction on the wind speed at WIFEH located on the windward
727   side of building with outdoor wind at U_H = 10 m/s

728   Fig. 23. Effect of wind direction on the wind speed at WIFEH located on the side of
729   building with outdoor wind at U_H = 10 m/s

730
731 Figure 24 illustrates the effect of different outdoor wind speed U_H values of 2, 4, 6, 8,
732 and 10 m/s at 0° wind direction on the air speed achieved at the device location. Similar
733 trend was observed for all the curves with the highest speed achieved in R1 and F3
734 and lowest speed achieved in F2 and S2. The increase in the velocity profile
735 corresponded to a proportional increased for the wind speed for all the device
736 locations.

737
738   Fig. 24. Wind speeds gathered at WIFEH position for various mounting locations for
739   0° wind angle of approach

740
741 Figure 25 depicts velocity results for 90° wind angle approach. At this angle the output
742 of the roof installations were overtaken by those in the front and side, most notably by
743 F3, S1 and S3 mainly because of the geometry of the device frame. The frame restricts
744 airflow in the perpendicular direction to the device. Therefore for locations with this
745 type of prevailing wind direction it will be better for the WIFEH to be integrated through
746 the front and side edges of the building.

747
748   Fig. 25. Wind speeds gathered at WIFEH position for various mounting locations for
749   90° wind angle of approach

750
751 Figure 26 compares the estimated output of the device at various locations and wind
752 directions of 0 to 90˚, in increments of 10 degrees while maintaining a uniform outdoor
753 wind velocity (U_H = 10 m/s). F1, F2 and F3 represent the WIFEH devices mounted on
754 the front face of the building; S1, S2 and S3 represent those on the side face, while
755 R1, R2 and R3 are those for the roof locations. As observed, the highest power output
756 comes from location R3 – the apex of the building – with an estimated output of 15.2
757 V, resulting from wind speed that accelerated up to approximately 14.4 m/s,
758 approximately 37.5% speed-up at the particular height. This occurred for an incoming
759 wind 30˚ relative to the building facade.

760
761 Depending on prevailing wind direction of the area, the installation location of the
762 device can be determined. The green trendline represents the power output trend for
763 R3, the location with the highest total power generation summed over 0 to 90 degrees.
764 The brown trendline shows the trend for S2, the location with the lowest summed power
765 generation over the same angular range.

766
767 Secondary to the building apex, locations on the edge also provide well above-average
768 power output. Based on the simulated conditions, locations S3, F1 and R1 should be
769 optimum locations for building integration of the WIFEH, considering the power
770 averages for 0, 45 and 90-degree orientations.

771
772 The last locations an installer would want to put an WIFEH on are the central areas of
773 the building's faces (illustrated by F2 and S2). Taking into account angular averages

these locations provided the least amount of power, with no power generated at all for some cases due to the wind speed not being able to make it to the WIFEH's cut-in wind speed for generation. This finding can be considered by some to be a counterintuitive result, considering these locations are directly hit by the oncoming wind.

Fig. 26. Sample calculation of estimated voltage output based on WIFEH (2-magnet-coil system)

Figure 27 compares the estimated output of the device located in the three locations F3, S3 and R3 at various outdoor wind speeds. Among these three locations, at 30° wind direction, R3 provided the highest output ranging between 2.5 to 15.2 V, while F3 showed the lowest output.

Fig. 27. Impact of various outdoor wind speeds (U_H) on the estimated output of the WIFEH for locations F3, S3 and R3

From the results it was clear that both the location of the device and wind direction had significant effects on the air speed achieved at the belt locations. Therefore a complete and detailed analysis of these factors should be carried out when integrating aero-elastic belts to buildings to ensure that the performance is optimised. Certain changes in angle exposure past certain critical values marked significant increase in velocity and consequently, power generation.

5. Conclusions and future works

The Wind-Induced Flutter Energy Harvester is valuable for low-energy wind harvesting in the built environment due to its low cost and modularity. The following points encapsulate the important findings of the study:

- With increasing airflow speed came increases in open-circuit voltage and short-circuit current produced by the WIFEH. Regular sinusoidal waveform voltage signals were observed through a digital oscilloscope for wind tunnel airflow speeds of 2.3 m/s and 5 m/s with the belt retensioned.
- The RMS (effective) voltages recorded were 3.0 V and 4.88 V with maximum values of 3.84 V and 9.20 V for 2.3 m/s and 5 m/s wind tunnel airflow speeds, respectively.
- The simulation used a gable-roof type building model with a 27˚ pitch obtained from the literature. The atmospheric boundary layer (ABL) flow was used for the simulation of the approach wind. At wind velocity (U_H) 4.7 m/s and 0° wind direction, the airflow speed in R1 was the highest for the roof section at 4.5 m/s. At wind velocity (U_H) 4.7 m/s and 0° wind direction, the airflow speed in F1 and F3 were the highest for the façade and side sections at 5.4 m/s.
- The overall highest power output comes from location R3 – the apex of the building – with an estimated output of 15.2 V, resulting from wind speed that accelerated up to approximately 14.4 m/s, approximately 37.5% speed-up at the particular height. This occurred for an incoming wind 30˚ relative to the building facade.

19

818   • Optimum installation of the WIFEH devices translates to prioritising the roof and
819   the trailing edges of the building to yield the highest possible power generation,
820   depending on wind conditions, while avoiding the leading edge or centres of
821   surfaces.
822

823 Future studies on the installation of the WIFEH in buildings will include simulations
824 using transient models that will also involve non-uniform flow conditions. Prospective
825 investigations on the impact of varying shapes of the subject building and different
826 locations of the device located on these new surfaces will also be conducted. Further
827 investigations will also include the impact of surrounding buildings on the performance
828 of the device. This will feature the shape of surrounding buildings, distance and
829 positioning, etc. Field tests will also be conducted to evaluate device performance in
830 actual conditions and assess other factors such as noise, visual and related
831 parameters. Economic analysis of the integration of the WIFEH in buildings will be
832 carried out and compared with more established low-energy generation technologies.
833

834 **NOMENCLATURE**

835 ***Symbols***
836 U Air velocity (m/s)
837 H Height (m)
838 k_s sand-grain roughness height (m)
839 c_s roughness constant
840 z_0 Aerodynamic roughness length (m)
841 F1, F2, F3   Front WIFEHs
842 S1, S2, S3   Side WIFEHs
843 R1, R2, R3   Roof WIFEHs
844

845

846 **Acknowledgement**
847

850

REFERENCES

[1] Pérez-Lombard, L., Ortiz, J., and Pout, C., "A review on buildings energy consumption information," *Energy and Buildings*, vol. 40, no. 3, pp. 394–398, 2008.

[2] Hu, Y., Zhang, Y., Xu, C., Lin, L., Snyder, R. L., and Wang, Z. L., "Self-powered system with wireless data transmission," *Nano Letters*, vol. 11, no. 6, pp. 2572–2577, Jun. 2011.

[3] Zhu, G., Yang, R., Wang, S., and Wang, Z., "Flexible high-output nanogenerator based on lateral ZnO nanowire array," *Nano Letters*, vol. 10, no. 8, pp. 3151–3155, 2010.

[4] Hu, Y., Zhang, Y., Xu, C., Zhu, G., and Wang, Z., "High-output nanogenerator by rational unipolar assembly of conical nanowires and its application for driving a small liquid crystal display," *Nano Letters*, vol. 10, no. 12, pp. 5025–5031, 2010.

[5] Arioli, G. and Gazzola, F., "A new mathematical explanation of what triggered the catastrophic torsional mode of the Tacoma Narrows Bridge," *Applied Mathematical Modelling*, vol. 39, no. 2, pp. 901–912, 2015.

[6] Wang, D., Chiu, C., and Pham, H., "Electromagnetic energy harvesting from vibrations induced by Kármán vortex street," *Mechatronics*, vol. 22, no. 6, pp. 746–756, 2012.

[7] Nguyen, H., Pham, H., and Wang, D., "A miniature pneumatic energy generator using Kármán vortex street," *Journal of Wind Engineering and Industrial Aerodynamics*, vol. 116, pp. 40–48, 2013.

[8] McCarthy, J., Watkins, S., and Deivasigamani, A., "An investigation of fluttering piezoelectric energy harvesters in off-axis and turbulent flows," *Journal of Wind Engineering and Industrial Aerodynamics*, vol. 136, pp. 101–113, 2015.

[9] Raghavan, K. and Bernitsas, M., "Experimental investigation of Reynolds number effect on vortex induced vibration of rigid circular cylinder on elastic supports," *Ocean Engineering*, vol. 38, no. 5, pp. 719–731, 2011.

[10] Norberg, C., "Fluctuating lift on a circular cylinder: review and new measurements," *Journal of Fluids and Structures*, vol. 17, no. 1, pp. 57–96, 2003.

[11] Sarpkaya, T., "A critical review of the intrinsic nature of vortex-induced vibrations," *Journal of Fluids and Structures*, vol. 19, no. 4, pp. 389–447,

887   2004.

[12] Tan, Y., Zhu, D., and Beeby, S., "Wind energy harvesting for recharging wireless sensor nodes: brief review and a case study," in *Rechargeable Sensor Networks: Technology, Theory, and Application*, 2014, pp. 1–30.

[13] Orrego, S., Shoele, K., Ruas, A., Doran, K., Caggiano, B., Mittal, R., and Kang, S. H., "Harvesting ambient wind energy with an inverted piezoelectric flag," *Applied Energy*, vol. 194, pp. 212–222, 2017.

[14] Xiong, H. and Wang, L., "Piezoelectric energy harvester for public roadway: On-site installation and evaluation," *Applied Energy*, vol. 174, pp. 101–107, 2016.

[15] Sue, C. Y. and Tsai, N. C., "Human powered MEMS-based energy harvest devices," *Applied Energy*, vol. 93, pp. 390–403, 2012.

[16] Yole Développement, "Emerging Energy Harvesting Devices," 2012.

[17] Han, N., Zhao, D., Schluter, J. U., Goh, E. S., Zhao, H., and Jin, X., "Performance evaluation of 3D printed miniature electromagnetic energy harvesters driven by air flow," *Applied Energy*, vol. 178, pp. 672–680, 2016.

[18] Pimentel, D., Musilek, P., Knight, A., and Heckenbergerova, J., "Characterization of a wind flutter generator," in *2010 9th Conference on Environment and Electrical Engineering, EEEIC 2010*, 2010, pp. 81–84.

[19] Arroyo, E., Foong, S., and Maréchal, L., "Experimental study of an omni-directional wind fluttering energy harvester," in *ASME 2014 Dynamic Systems and Control Conference*, 2014, p. V003T53A002-V003T53A002.

[20] Dinh Quy, V., Van Sy, N., Tan Hung, D., and Quoc Huy, V., "Wind tunnel and initial field tests of a micro generator powered by fluid-induced flutter," *Energy for Sustainable Development*, vol. 33, pp. 75–83, 2016.

[21] Fei, F., Mai, J., and Li, W., "A wind-flutter energy converter for powering wireless sensors," *Sensors and Actuators A: Physical*, vol. 173, no. 1, pp. 163–171, 2012.

[22] Zhu, D., Beeby, S., Tudor, J., White, N., and Harris, N., "A novel miniature wind generator for wireless sensing applications," in *Sensors, 2010 IEEE*, 2010, pp. 1415–1418.

[23] Wang, X., Pan, C. C. L., Liu, Y. Y. Bin, and Feng, Z. H., "Electromagnetic resonant cavity wind energy harvester with optimized reed design and effective magnetic loop," *Sensors and Actuators, A: Physical*, vol. 205, pp.

921   63–71, 2014.

[24] Kim, S. S., Ji, C., Galle, P., Herrault, F., Wu, X., Lee, J., Choi, C., and Allen, M. G., "An electromagnetic energy scavenger from direct airflow," *Journal of Micromechanics and Microengineering*, vol. 19, no. 9, p. 94010, 2009.

[25] Munaz, A. and Chung, G.-S., "An electromagnetic energy harvester based on multiple magnet scavenging power from low frequency vibration," *Microsystem Technologies*, pp. 1–9, 2015.

[26] Kwon, S., Kim, K., and Lee, S., "Energy Harvesting from Aeroelastic Flutter," in *The 2012 World Congress on Advances in Civil, Environmental, and Materials Research (ACEM' 12)*, 2012.

[27] Park, J., Kim, K., Kwon, S., Law, K. H., and Engineering, C., "An aeroelastic flutter based electromagnetic energy harvester with wind speed augmenting funnel," in *Proceedings of the International Conference on Advances in Wind and Structures*, 2012, pp. 26–29.

[28] Arroyo, E., Foong, S., and Wood, K. L., "Modeling and experimental characterization of a fluttering windbelt for energy harvesting," *Journal of Physics: Conference Series*, vol. 557, no. 1, p. 12089, 2014.

[29] Toja-Silva, F., Peralta, C., Lopez-Garcia, O., Navarro, J., and Cruz, I., "On Roof Geometry for Urban Wind Energy Exploitation in High-Rise Buildings," *Computation*, vol. 3, no. 2, pp. 299–325, 2015.

[30] Calautit, J. K., Chaudhry, H. N., Hughes, B. R., and Sim, L. F., "A validated design methodology for a closed-loop subsonic wind tunnel," *Journal of Wind Engineering and Industrial Aerodynamics*, vol. 125, pp. 180–194, 2014.

[31] Sofotasiou, P., Calautit, J. K., Hughes, B. R., and O'Connor, D., "Towards an integrated computational method to determine internal spaces for optimum environmental conditions," *Computers & Fluids*, vol. 127, pp. 146–160, 2016.

[32] Tominaga, Y., Akabayashi, S., Kitahara, T., and Arinami, Y., "Air flow around isolated gable-roof buildings with different roof pitches: Wind tunnel experiments and CFD simulations," *Building and Environment*, vol. 84, pp. 204–213, 2015.

[33] Franke, J., Hellsten, A., Schlünzen, H., Carissimo, B., Baklanov, A., Barmpas, P., Bartzis, J., Batchvarova, E., Baumann-Stanzer, K., Berkowicz, R., Borrego, C., Britter, R., Brzozowski, K., Burzynski, J., Margarida Costa, A., Dimitrova, R., Grawe, D., Goricsan, I., Janour, Z., Karppinen, A.,

Ketzel, M., Krajcovicova, J., Leitl, B., Martilli, A., Moussiopoulos, N., Neophytou, M., Olesen, H., Papachristodoulou, C., Papadakis, M., Piringer, M., Di Sabatino, S., Sandberg, M., Schatzmann, M., and Trini-Castelli, S., "Best practice guideline for the CFD simulation of flows in the urban environment," 2007.

[34] Chaudhry, H., Calautit, J., and Hughes, B., "Computational analysis of a wind tower assisted passive cooling technology for the built environment," *Journal of Building Engineering*, vol. 1, pp. 63–71, 2015.

[35] Calautit, J. and Hughes, B., "Wind tunnel and CFD study of the natural ventilation performance of a commercial multi-directional wind tower," *Building and Environment*, vol. 80, pp. 71–83, 2014.

[36] Calautit, J., O'Connor, D., and Hughes, B., "Determining the optimum spacing and arrangement for commercial wind towers for ventilation performance," *Building and Environment*, vol. 82, pp. 274–287, 2014.

[37] Roache, P., "Conservatism of the GCI in Finite Volume Computations on Steady State Fluid Flow and Heat Transfer," *ASME J. Fluids Eng.*, vol. 125, pp. 731–732, 2003.

[38] Celik, I., Ghia, U., and Roache, P., "Procedure for estimation and reporting of uncertainty due to discretization in {CFD} applications," *Journal of fluids {Engineering-*, 2008.

[39] Roache, P., "A method for uniform reporting of grid refinement studies," *ASME-PUBLICATIONS-FED*, 1993.

[40] Tominaga, Y., Mochida, A., Yoshie, R., Kataoka, H., Nozu, T., Yoshikawa, M., and Shirasawa, T., "AIJ guidelines for practical applications of CFD to pedestrian wind environment around buildings," *Journal of Wind Engineering and Industrial Aerodynamics*, vol. 96, no. 10–11, pp. 1749–1761, 2008.

[41] Launder, B. and Spalding, D., "The numerical computation of turbulent flows," *Computer methods in applied mechanics and engineering*, vol. 3, no. 2, pp. 269–289, 1974.

[42] Cebeci, T. and Bradshaw, P., *Momentum transfer in boundary layers*. Washington, DC, Hemisphere Publishing Corp.; New York, McGraw-Hill Book Co, 1977.

[43] Blocken, B., Stathopoulos, T., and Carmeliet, J., "CFD simulation of the atmospheric boundary layer: wall function problems," *Atmospheric environment*, vol. 41, no. 2, pp. 238–252, 2007.

24

Table 1. Sample calculations of discretisation error using the GCI method

	Velocity at height = 3.024m	Velocity at height = 3.021m	Velocity at height = 3.012m
C_1, C_2, C_3	5.9 million, 3.5 million, 2million elements	5.9 million, 3.5 million, 2million elements	5.9 million, 3.5 million, 2million elements
r_{21}	1.29835	1.29835	1.29835
r_{32}	1.3228	1.3228	1.3228
$\emptyset_1$	2.7134	4.44694	3.73981
$\emptyset_2$	2.80474	4.44386	3.7654
$\emptyset_3$	2.9764	4.39079	3.74622
p	2.0689	10.1268	1.0609
$\emptyset_{ext}^{21}$	2.5859	4.4472	3.6596
e_a^{21}	3.36%	0.070%	0.68%
e_{ext}^{21}	2.58%	0.005%	2.19%
GCI_{fine}^{21}	5.87%	0.007%	2.68%

Table 2. Summary of the CFD model boundary conditions

Boundary condition	Set value
Algorithm	SIMPLE
Time	Steady state
Solver type	Pressure based
Discretisation Scheme	Second order upwind
Turbulence model	Standard k-epsilon
Wall boundaries	Standard wall functions
Wall boundaries (Ground)	Modified for roughness Roughness height K_s (m): 0.001 Roughness constant C_{Ks}: 0.5
	Macro-micro climate walls: 0.001
Wall (Sides)	Symmetry (zero normal velocity and zero gradients)
Wall (Top)	Symmetry (zero normal velocity and zero gradients)
Velocity inlet (m/s) at UH	2-10
Wind angle (˚)	0-90
Pressure outlet (Pa)	0 (atmospheric)

Gravity (m/s^2)	-9.81

999
1000

1001
1002
1003
1004
1005
1006
1007
1008
1009
1010
1011
1012
1013
1014
1015
1016
1017
1018
1019
1020
1021
1022
1023
1024
1025
1026
1027
1028
1029
1030
1031
1032
1033
1034
1035
1036
1037
1038
1039
1040
1041
1042
1043
1044
1045

1046
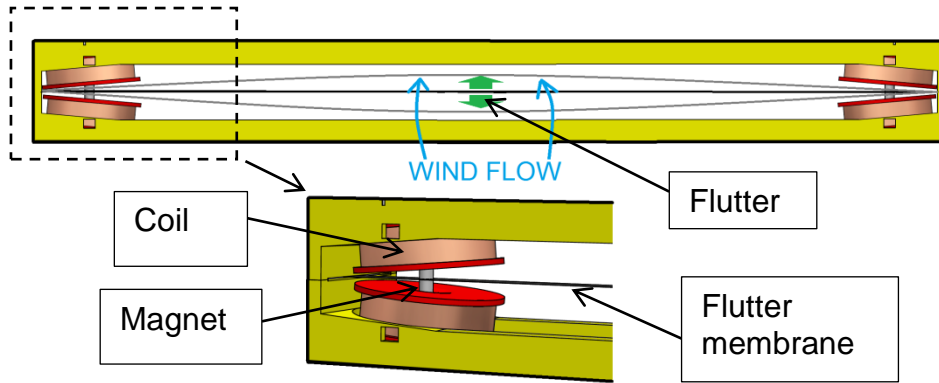
WIND FLOW

Flutter

Coil

Magnet

Flutter membrane

1047
1048
1049 Fig. 1. Schematic diagram of a quad (4-coil arrangement) Wind-Induced Flutter
1050 Energy Harvester (WIFEH)
1051
1052

1053
1054
1055 Fig. 2. General organisation of the study
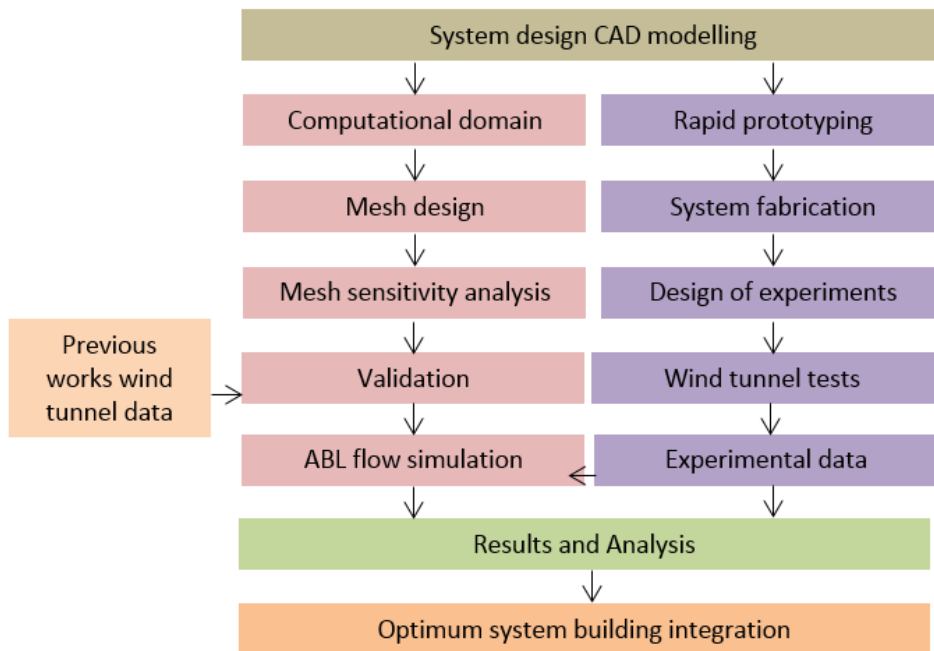
1056
1057
1058
1059
1060
1061
1062
1063
1064

Fig. 3. (a) Side view of the closed-loop wind tunnel (b) WIFEH prototype with one coil configuration showing flutter motion at 2.3 m/s
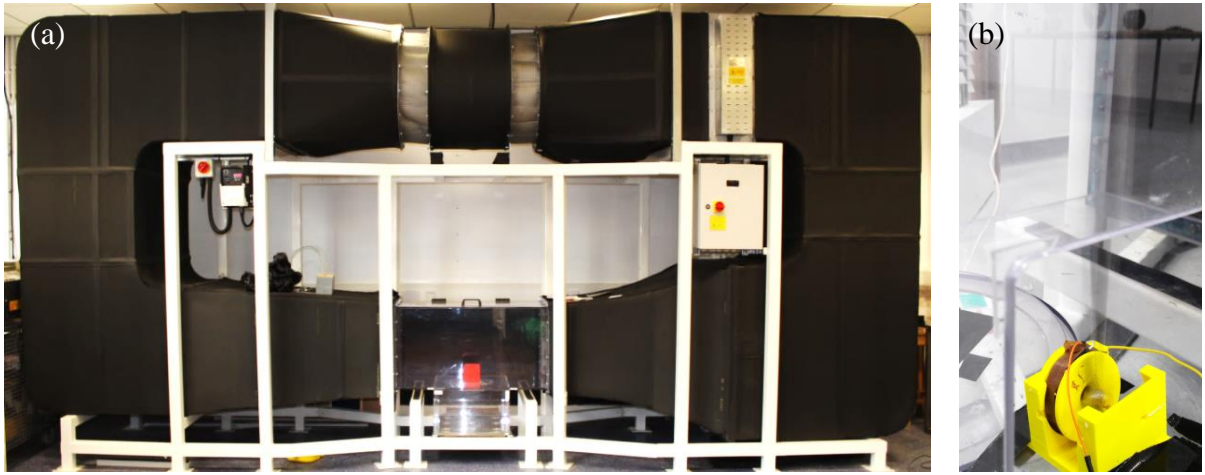
Fig. 4. Schematic of WIFEH prototype in the wind tunnel test section

.
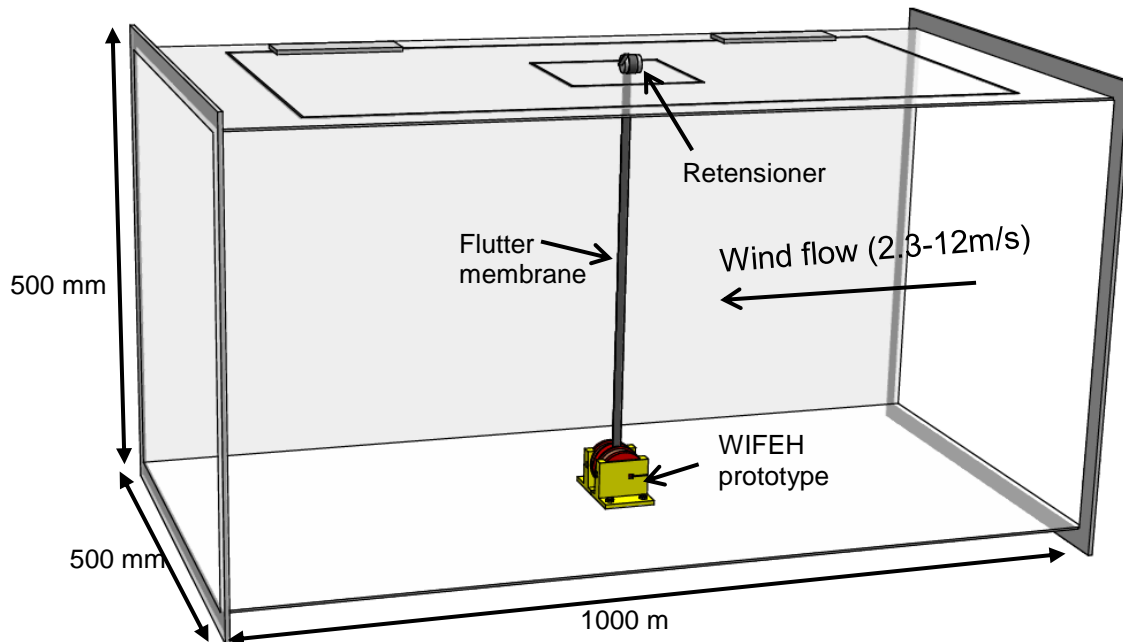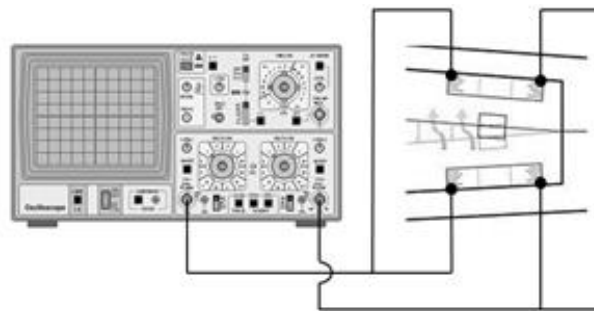
Fig. 5. Schematic of the coil connections to the oscilloscope

1078
1079
1080
1081
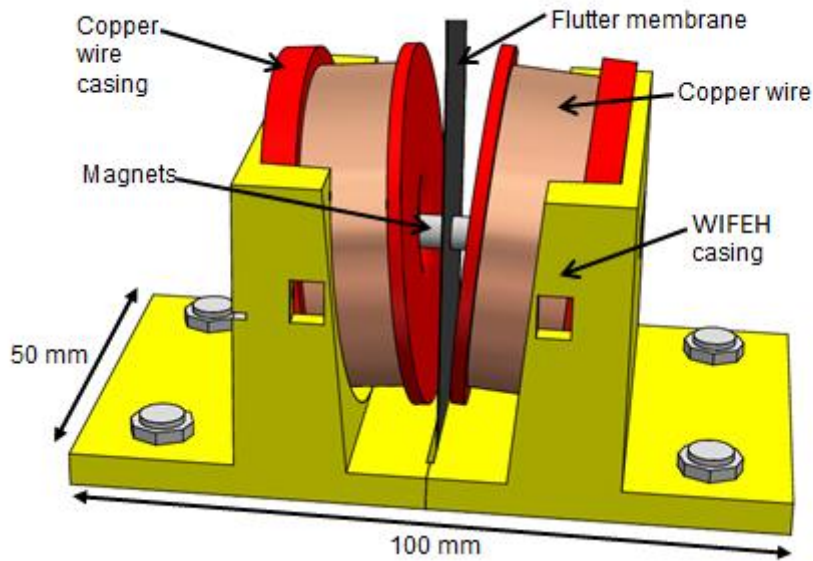
1082
1083 Fig. 6. Schematic and dimensions of 3D-printed WIFEH prototype
1084
1085
1086
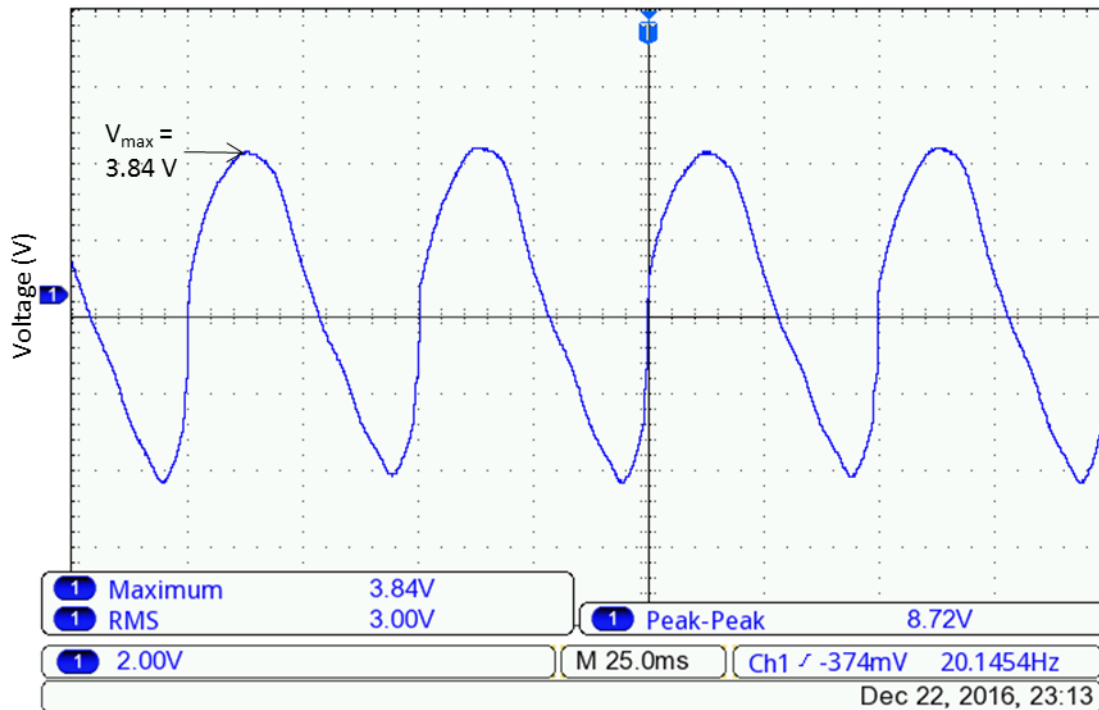
1087
1088 Fig. 7. Open-circuit voltage of the Wind-Induced Flutter Energy Harvester (WIFEH)
1089 without membrane retensioning under 2.3 m/s flow velocity
1090
1091
1092

1093
1094
1095
1096

$V_{max} = 8.80$ V

1	Maximum	8.80V		1	Peak-Peak	18.4V
1	RMS	4.16V
1	5.00V		M 25.0ms		Ch1 ∕ -374mV	20.5246Hz
						Dec 22, 2016, 23:16

Voltage (V)

1097
1098   Fig. 8. Electrical signal open-circuit voltage of the Wind-Induced Flutter Energy
1099   harvester (WIFEH) without membrane retensioning under 5m/s flow velocity
1100
1101

$V_{max} = 9.20$ V

1	Maximum	9.20V		1	Peak-Peak	18.2V
1	RMS	4.88V
1	5.00V		M 25.0ms		Ch1 ∕ -374mV	28.3741Hz
						Dec 22, 2016, 23:18

Voltage (V)

1102
1103

30

1104   Fig. 9. Electrical signal open-circuit voltage of the Wind-Induced Flutter Energy
1105   Harvester (WIFEH) with membrane retensioning under 5 m/s flow velocity
1106

1107
1108   Fig. 10. Electrical output performance of the WIFEH without retensioning under
1109   various flow velocities: (a) Open-circuit voltage (b) Short-circuit current
1110
1111
1112
1113

1114
1115   Fig. 11. Electrical output performance of the WIFEH with retensioning under various
1116   flow velocities: (a) Open-circuit voltage (b) Short-circuit current
1117
1118
1119

Fig. 12. CAD geometry of building with WIFEH devices

Fig. 13. Computational domain of building with WIFEH devices

Fig. 14. (a) Computational grid (b) Sensitivity analysis

1131
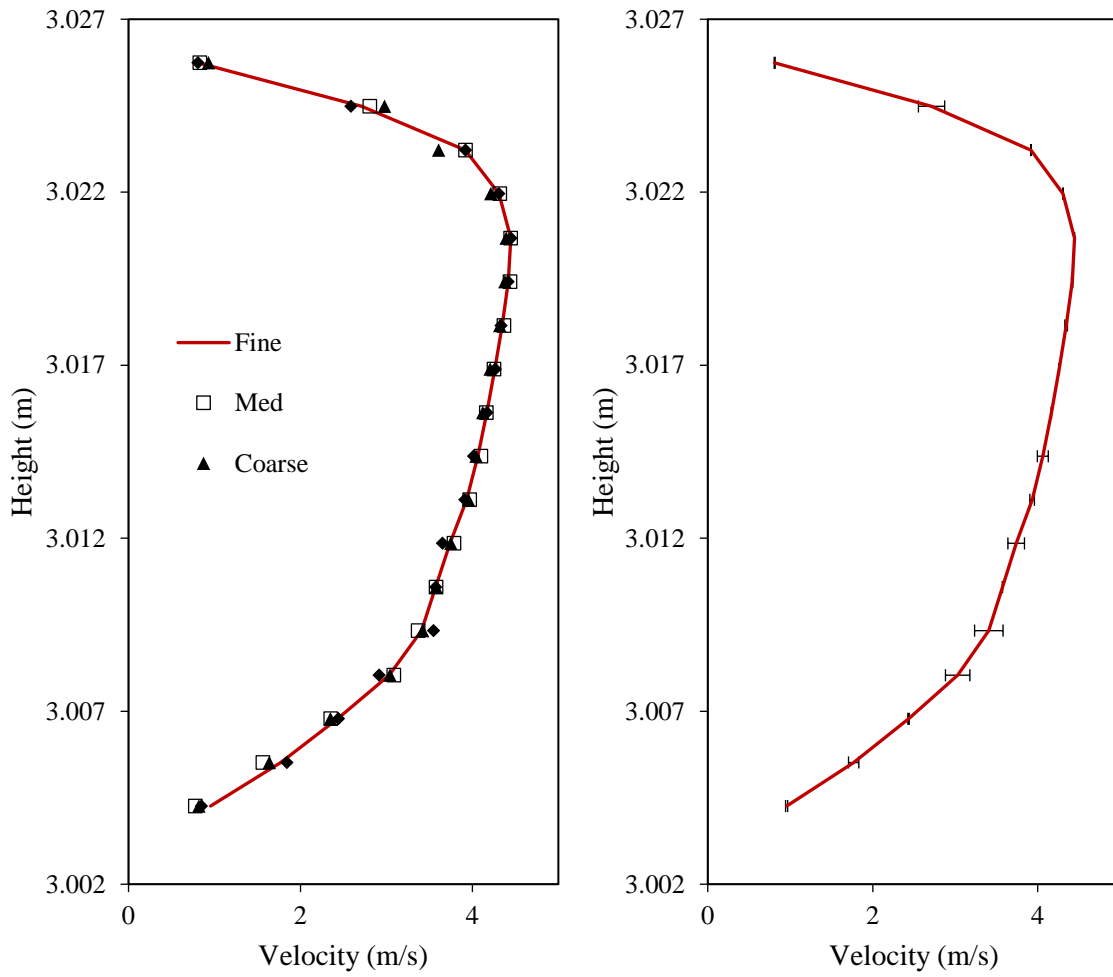
1132
1133
1134 Fig. 15. Grid verification using the Grid Convergence (GCI) method. (a) plot of the
1135   velocity profiles drawn from a line in the R1 device; (b) fine grid solution, with
1136   discretisation error bars computed using the GCI index.
1137
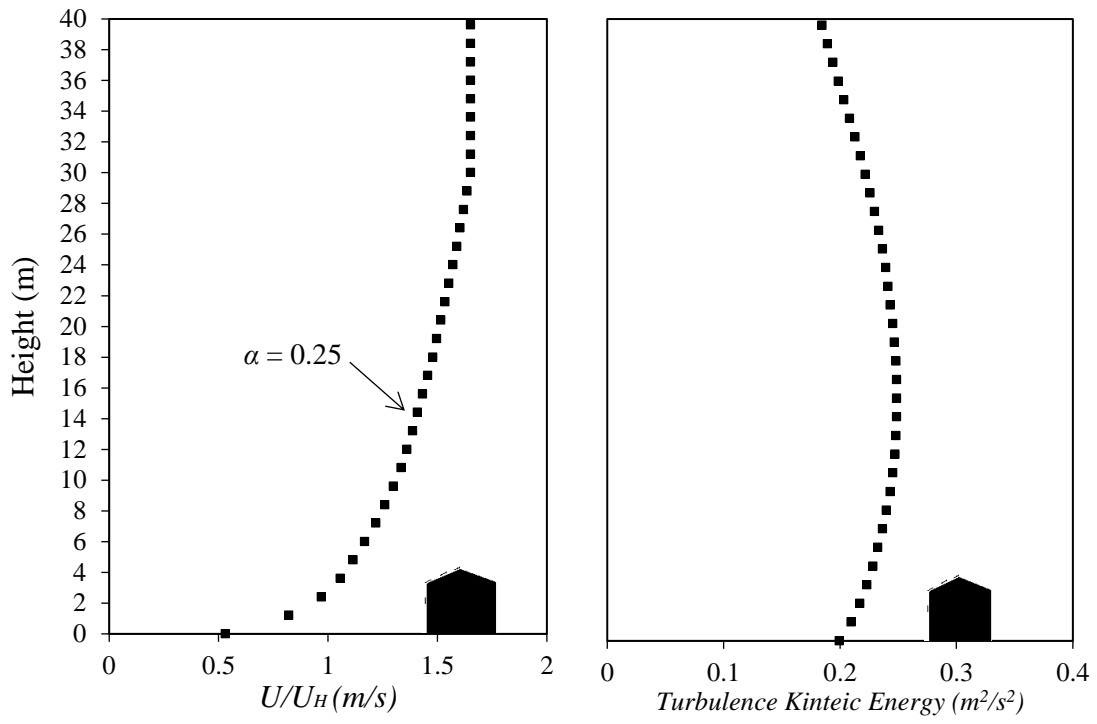
Fig. 16. (a) Velocity profile (b) TKE profile of approach wind flow [29]

1143
1144
1145
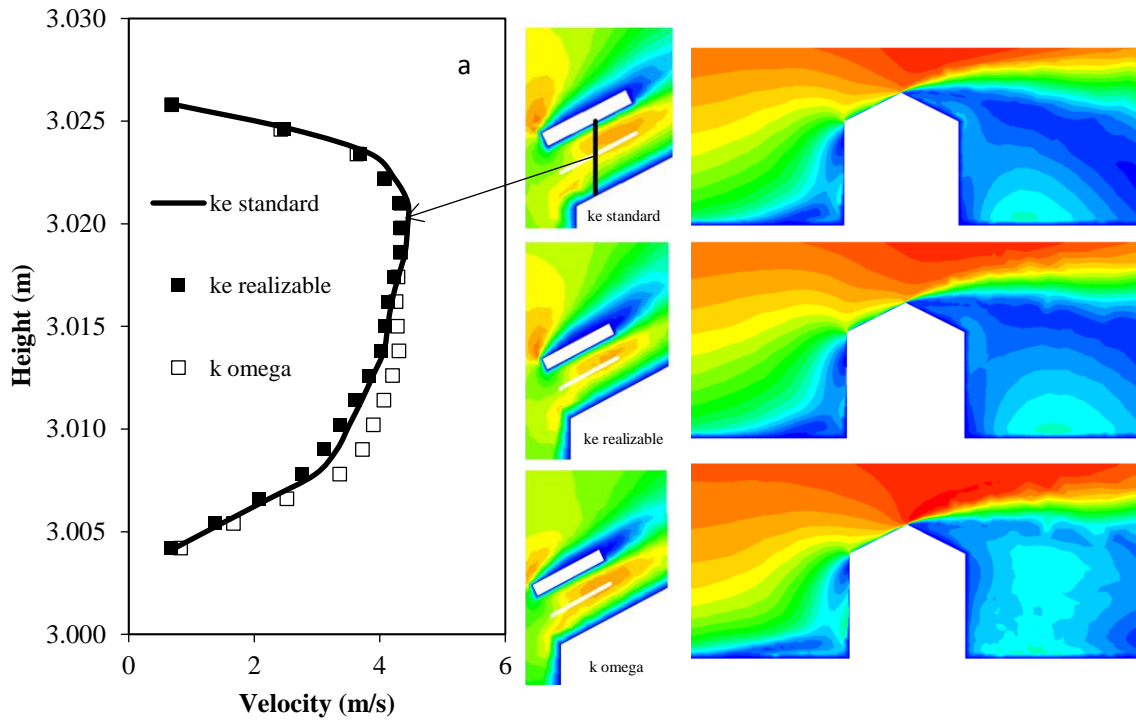
1146
1147
1148 Fig. 17. Sensitivity analysis of turbulence model (a) velocity profile in R1 (b) velocity
1149 contours
1150
1151
1152
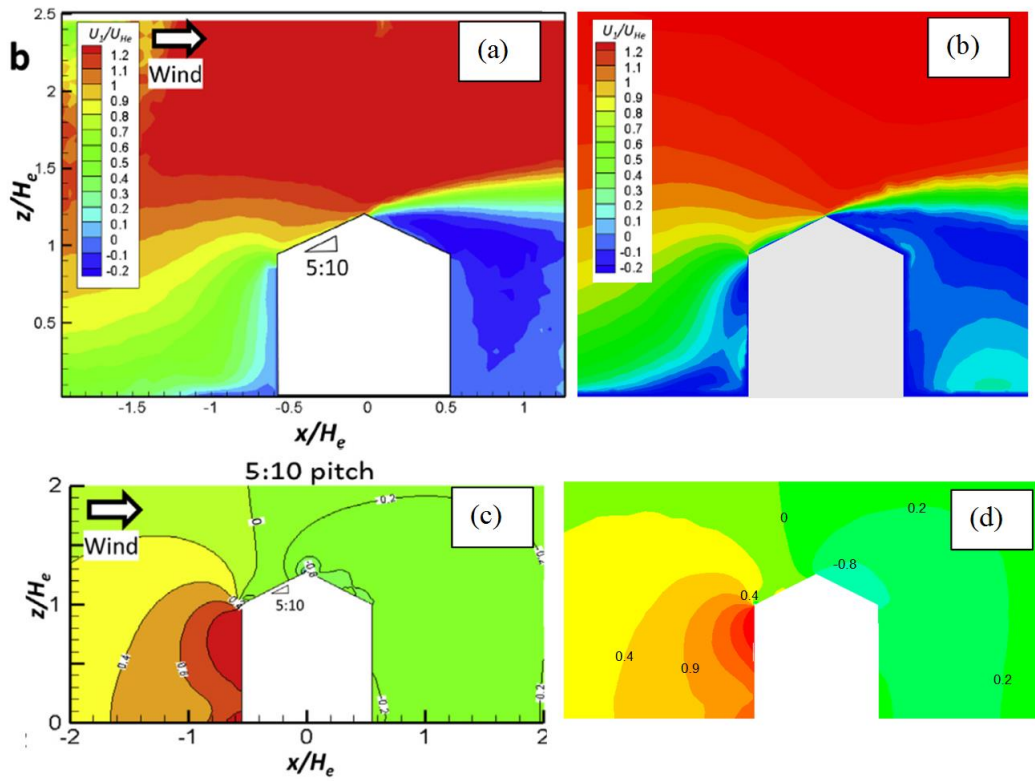
Fig. 18. (a) PIV measurements of velocity [29] (b) velocity distribution in the current model (c) pressure coefficient result [29] (d) pressure coefficient distribution in the current model
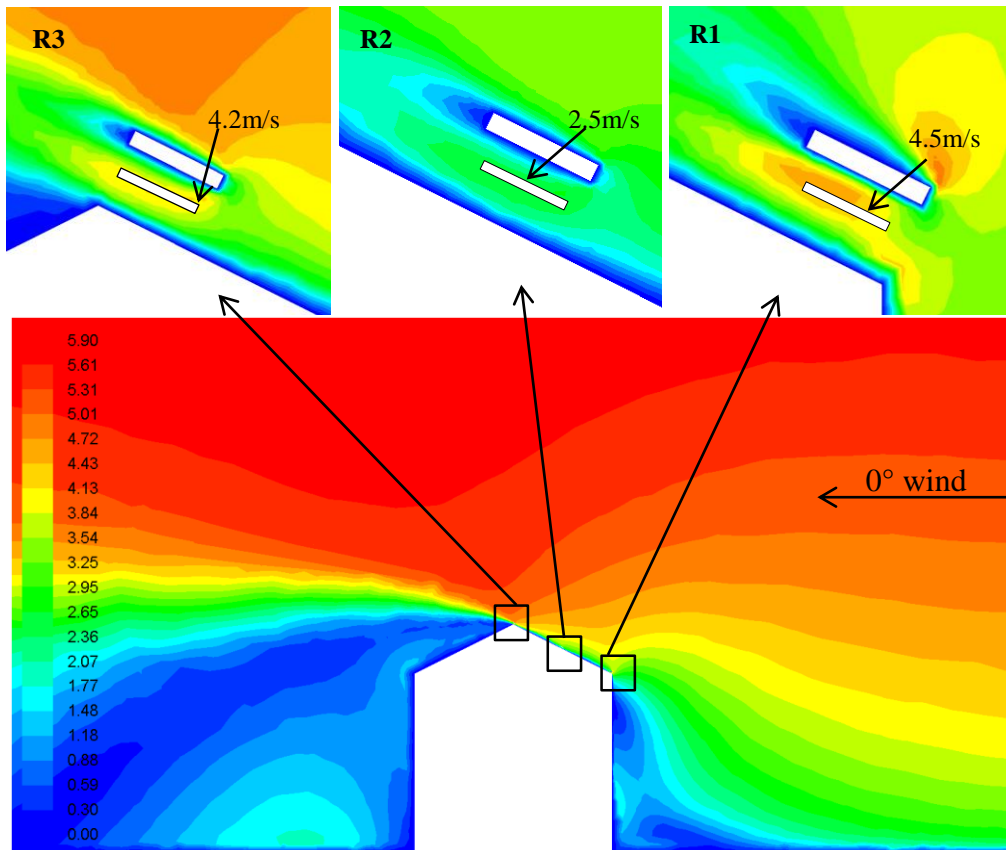
1160 Fig. 19. Contours of velocity magnitude showing a cross-sectional side view of the
1161   building
1162
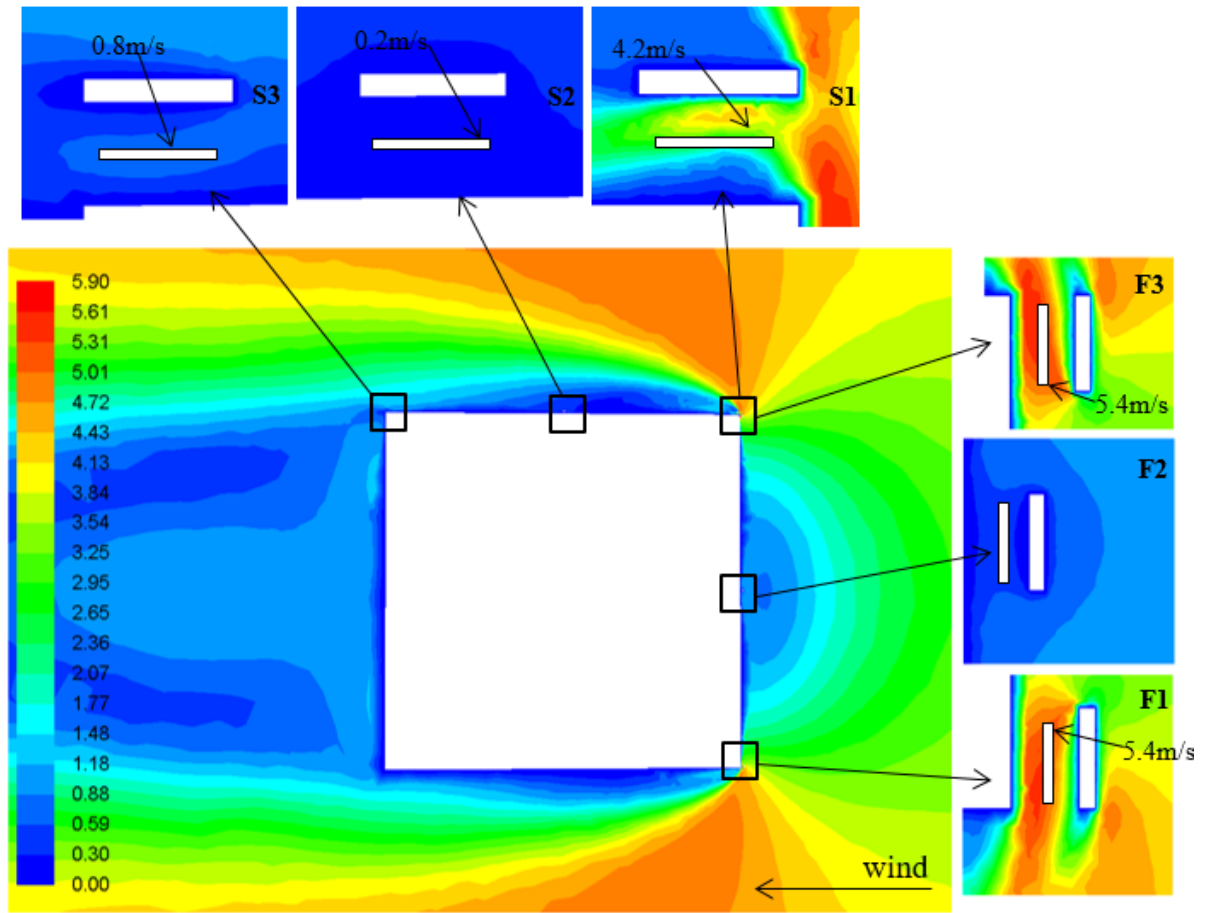
1163

1164 Fig. 20. Contours of velocity magnitude showing a cross-sectional top view of the
1165   building

1166
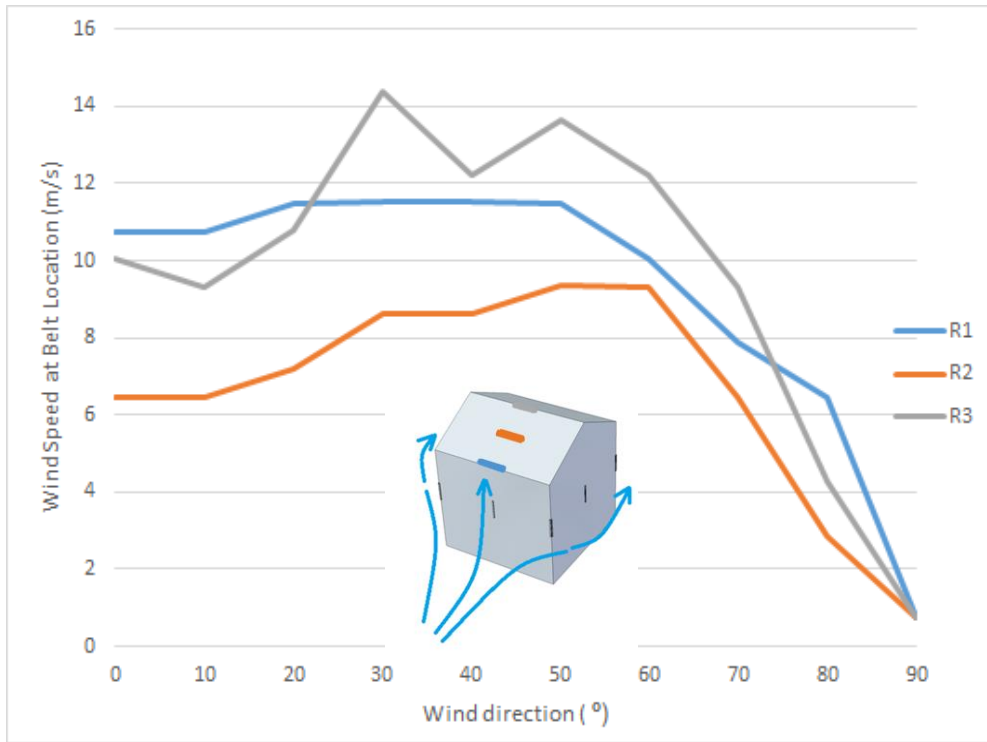
1167

1168 Fig. 21. Effect of wind direction on the wind speed at WIFEH located on the roof for
1169 various wind angle of approach with outdoor wind U_H = 10 m/s

1170
1171
1172
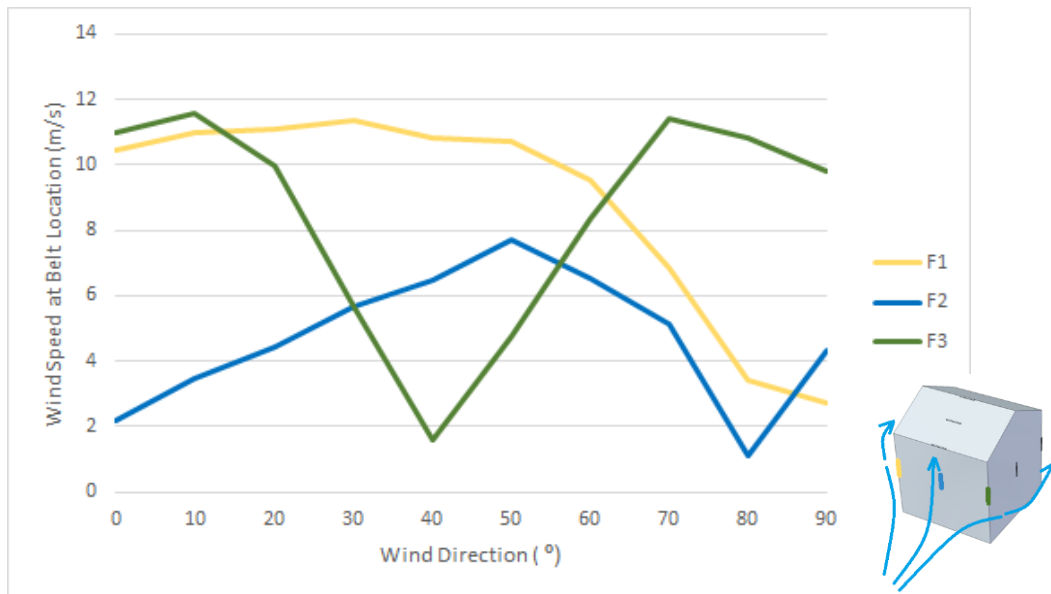
1173

1174 Fig. 22. Effect of wind direction on the wind speed at WIFEH located on the windward
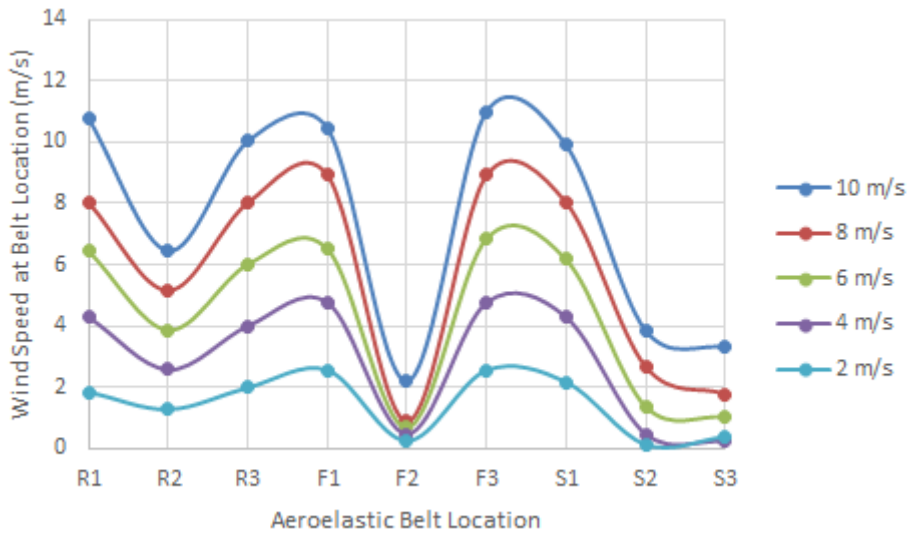1175 side of building with outdoor wind at U_H = 10 m/s
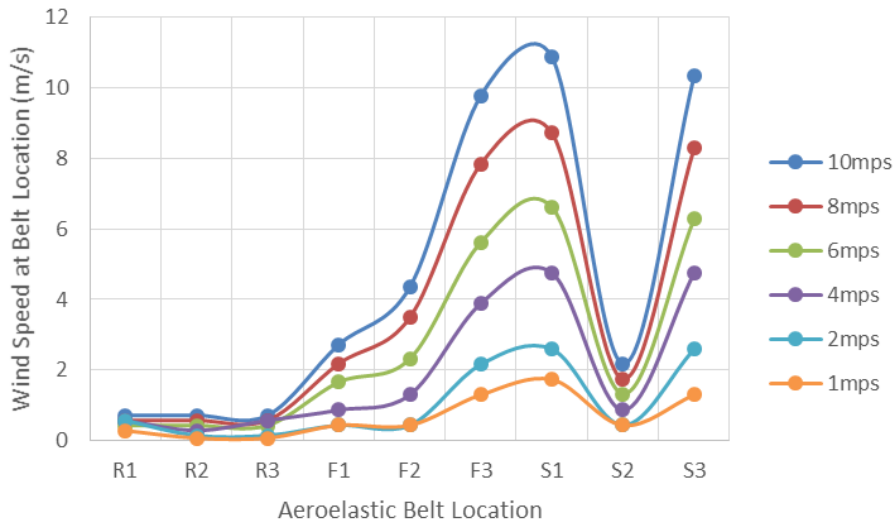
1176
1177
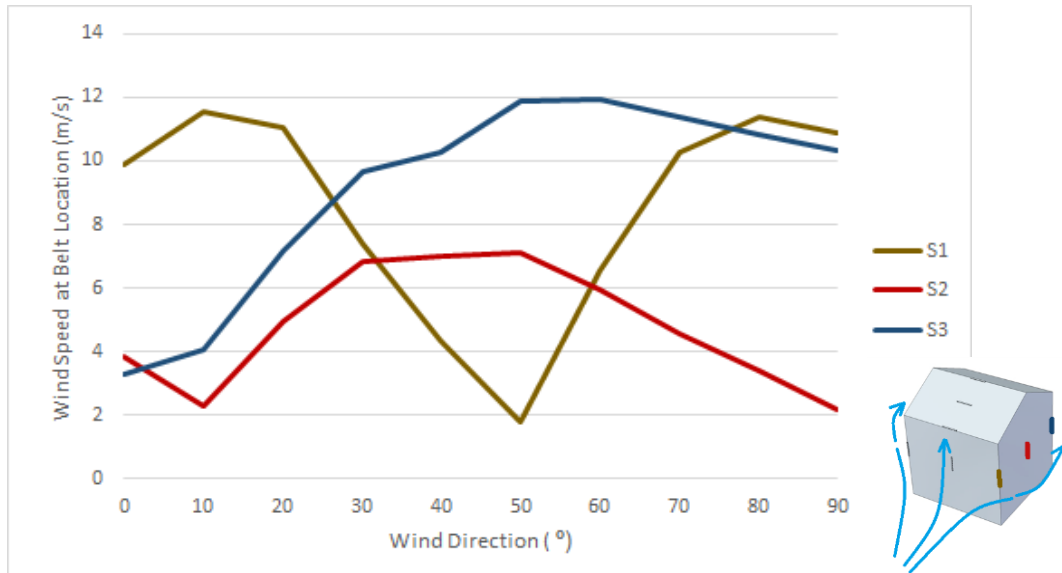
39

1178
1179

1180   Fig. 23. Effect of wind direction on the wind speed at WIFEH located on the side of
1181   building with outdoor wind at U_H = 10 m/s
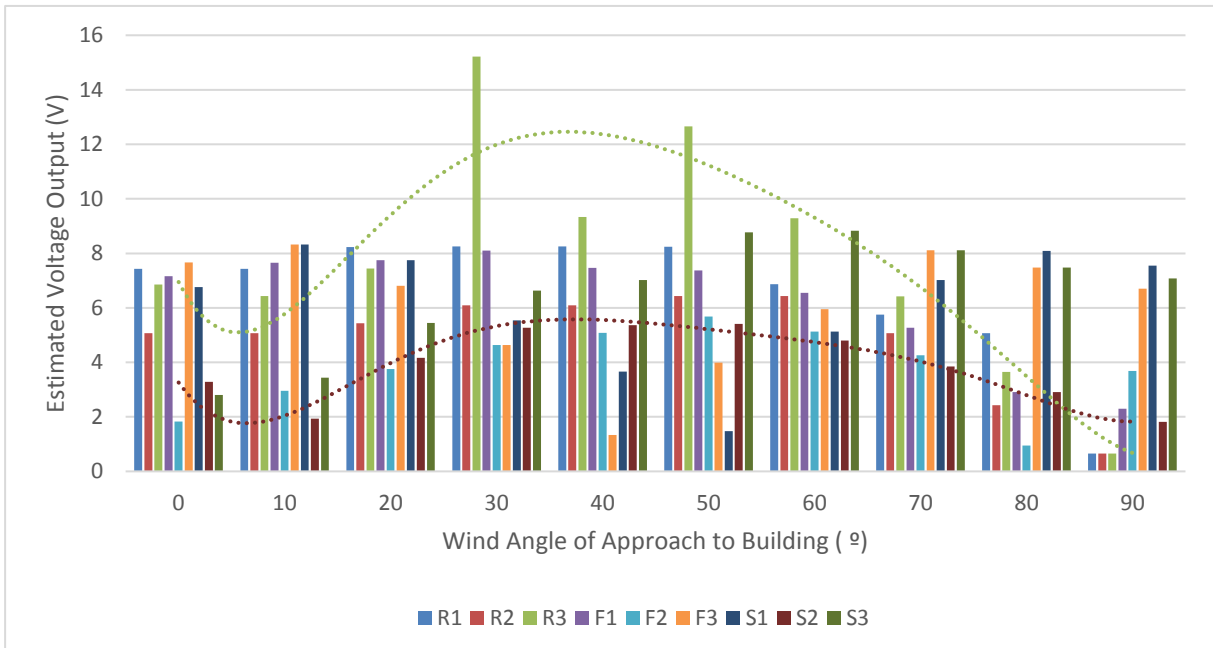
1182
1183
1184
1185
1186

1187
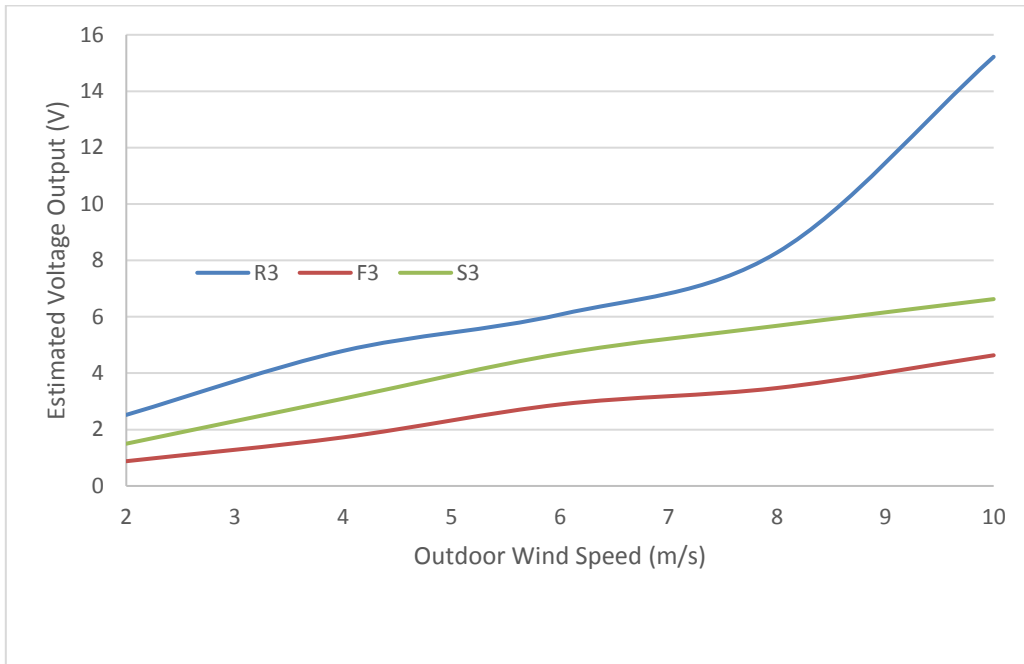1188   Fig. 24. Wind speeds gathered at WIFEH position for various mounting locations for
1189   0° wind angle of approach
1190

Fig. 25. Wind speeds gathered at WIFEH position for various mounting locations for 90° wind angle of approach

Fig. 26. Sample calculation of estimated voltage output based on WIFEH (2-magnet-coil system)

1200

1201   Fig. 27. Impact of various outdoor wind speeds (U_H) on the estimated output of the
1202   WIFEH for locations F3, S3 and R3

1203
1204
1205
1206
1207